

MODELING AND SIMULATION OF THERMO-FLUID-ELECTROCHEMICAL ION FLOW IN BIOLOGICAL CHANNELS

RICCARDO SACCO¹, FABIO MANGANINI², AND JOSEPH W. JEROME³

ABSTRACT. In this article we address the study of ion charge transport in the biological channels separating the intra and extracellular regions of a cell. The focus of the investigation is devoted to including thermal driving forces in the well-known velocity-extended Poisson-Nernst-Planck (vPNP) electrodiffusion model. Two extensions of the vPNP system are proposed: the velocity-extended Thermo-Hydrodynamic model (vTHD) and the velocity-extended Electro-Thermal model (vET). Both formulations are based on the principles of conservation of mass, momentum and energy, and collapse into the vPNP model under thermodynamical equilibrium conditions. Upon introducing a suitable one-dimensional geometrical representation of the channel, we discuss appropriate boundary conditions that depend only on effectively accessible measurable quantities. Then, we describe the novel models, the solution map used to iteratively solve them, and the mixed-hybrid flux-conservative stabilized finite element scheme used to discretize the linearized equations. Finally, we successfully apply our computational algorithms to the simulation of two different realistic biological channels: 1) the Gramicidin-A channel considered in [10]; and 2) the bipolar nanofluidic diode considered in [40].

1. INTRODUCTION AND MOTIVATION

Ion channels are ubiquitous in the cells of the human body. They allow communication between the intra and extra-cellular sites and are responsible for the signaling pathways that regulate the activity of each part of the body system. A complete presentation of ionic channels is far beyond the scope of this article. For a treatment of the general properties of ionic channels and of their characterization in cellular biology and neuroscience we refer to the books [16] and [13]. In broad terms, ion channel are “biological gates” that can be activated (opened) or deactivated (closed) by the application of electrical, chemical, mechanical or thermal stimuli.

In the present article we mainly focus on the interaction among electrical, chemical and thermal driving forces, starting from the evidence that the sensory system in mammals is capable of discriminating thermal stimuli ranging from noxious cold ($< 8^\circ\text{C}$) to noxious heat ($> 52^\circ\text{C}$). Of particular relevance are the biological temperature sensors denoted thermo-transient receptor potential (thermo-TRP) cation channels. Thermo-TRP channels constitute a “superfamily” of receptors in sensory neurons that can be activated by noxious stimuli, resulting in the transmission to the spinal cord and brain of the information of local pain perception [14]. The fact that the thermal thresholds of many thermo-TRP channels can be modulated by extracellular mediators has recently led to the development of antagonists for noxious channel blockage in therapeutic uses as novel analgesics [39]. This is the case, for example, of heat-sensitive TRP channels exposed to capsaicin, a natural ingredient of spicy

Date: April 24, 2015.

foods such as red hot chilli peppers and of cold-sensitive TRP channels exposed to menthol. In [7] and [41], it is shown how the chemical agonists capsaicin and menthol function for both types of TRP channels as gating modifiers, shifting activation curves towards physiological membrane potentials.

Despite a significant amount of experimental data, the mechanisms underlying the marked temperature sensitivity of channel gating are still largely unknown. For this reason, the use of mathematical tools is increasingly becoming popular to support biophysical conjectures and suggest novel theories for data interpretation.

In this context, the most widely adopted approach to ion channel modeling and simulation is represented by compartmental models described by a system of ordinary differential equations (ODEs) based on the solution of Kirchhoff current law (KCL) written at the cellular membrane level [22]. The KCL equation is supplemented by phenomenological expressions characterizing the input-output functional response of each protein channel to changes in ion concentrations and/or electric potential inside and outside the cell [16]. Temperature in these models is usually assumed to be a given parameter.

More sophisticated approaches involve the solution of a system of partial differential equations (PDEs) expressing balance of mass of each single ion species flowing across the channel and the Gauss law for the electric field. The system is supplemented by a transport relation, known as the Nernst-Planck (NP) equation, that describes ion motion under an electrochemical gradient [31, 19, 17]. Also in this kind of modeling, well-known as the Poisson-Nernst-Planck (PNP) system and as the Drift-Diffusion (DD) system [25, 18], temperature is a given parameter.

A significant step forward to account for temperature as a dependent variable was taken in [10]. In this reference a hydrodynamic (HD) formulation including convective and thermal energy in the electro-chemical motion of a single cation is proposed and numerically investigated. A remarkable feature of [10] is that model and analysis are inspired and guided by the analogy between a biological ion channel and the channel of a semiconductor device in which electrons and holes, instead of charged ion particles, flow to transport electrical current between device terminals. This similarity between biology and solid-state electronics has been thoroughly addressed in the overview paper [12], in the numerical simulations of [15, 17, 28] and in the MSc thesis [24]. In this latter reference, the mathematical view of [10] is generalized by the introduction of a hierarchical modeling perspective to represent ion transport in a biological channel in which the interstitial electrolyte fluid is assimilated to the semiconductor device medium where two monovalent species (anion and cation) are flowing under the effect of electric, chemical and thermal forces. The hierarchy proposed in [24] is based on the ideas discussed in the semiconductor modeling reference books [36], [26], [18] and [21], and includes four members: the basic DD formulation, the electro-thermal (ET) formulation, the hydrodynamic (HD) formulation and the thermo-hydrodynamic (THD) formulation. For each member of the hierarchy, a set of conservation laws for mass, momentum and energy is written. In the case of DD, ET and HD models, the energy exchange between particles and medium are neglected while in the case of the THD model a supplementary conservation law is added to account for the dynamical thermo-electrochemical balance among the three interacting subsystems. The hierarchy is extensively investigated in a series of numerical computations performed in a

simplified one-dimensional channel geometry. Externally applied data on which a sensitivity analysis is carried out are the values of bulk ion concentrations in the intra and extra-cellular sites and the applied potential drop across the channel. Simulations indicate that: *i*) channel heating is, in general, relatively small compared to ion heating; and *ii*) for certain ranges of model parameters, the high-order effects introduced by the THD picture can significantly affect the input-output transfer characteristics of the “biological transistor”.

Based on the experience and results described above, in the present article we propose the following mathematical structure for the modeling of ion charge transport in biological channels:

- (a): in Section 2 we review the classic DD (PNP) model for ion electrodiffusion;
- (b): in Section 3 we use the channel conformation model proposed in [9] to supply the DD (PNP) formulation with a set of “reduced order” boundary conditions that allow one to account for the experimentally accessible values of applied bias, ion concentrations and bathing temperatures;
- (c): in Section 4 we review two members of the hierarchy of models for ion charge transport introduced in [24], the Thermo-Hydrodynamic and Electro-Thermal systems, and include electroosmotic effects by adding a linear advective term into the momentum balance equations proportional to the given electrolyte fluid velocity. The resulting modified hierarchy is a family of (approximated) velocity-extended models, as the self-consistent study of electrolyte fluid dynamics through Navier-Stokes equations is neglected unlike in [31, 19, 20, 35];
- (d): in Section 5 we illustrate the solution map used to solve iteratively the models in (a), (b) and (c) in steady-state conditions;
- (e): in Section 6 we study a linear model advective-diffusive and reactive boundary value problem (BVP) that represents each of the subproblems arising in the solution map, focusing on the continuous maximum principle;
- (f): in Section 7 we address the numerical study of the model BVP in (e) based on the dual-mixed hybridized (DMH) finite element method proposed and analyzed in [3, 5, 29] for elliptic equations and extended to more general differential operators in [2];
- (g): in Section 8 we propose a stabilization of the DMH scheme to deal with the case where advection or reaction dominate over diffusion in the model BVP;
- (h): in Section 9 we conduct a series of numerical tests to verify the convergence and stability properties of the DMH method;
- (i): in Section 10 we apply external temperature gradients, besides the usual electrochemical gradients, to the biological transistor to replicate *in vitro* the biophysical situations occurring *in vivo* in thermo-TRP channels;
- (j): in the concluding Section 11 we summarize the main contributions of the present research and we address a list of forthcoming activities for model improvement.

2. THE POISSON-NERNST-PLANCK MODEL FOR ION ELECTRODIFFUSION

The Poisson-Nernst-Planck system (PNP) for ion electrodiffusion reads [31]:

$$\begin{aligned}
(1a) \quad & \frac{\partial c_i}{\partial t} + \operatorname{div} \mathbf{f}_i(c_i, \varphi) = 0 & i = 1, \dots, M \\
(1b) \quad & \mathbf{f}_i(c_i, \varphi) = -D_i \nabla c_i + \mu_i \frac{z_i}{|z_i|} c_i \mathbf{E} & i = 1, \dots, M \\
(1c) \quad & D_i = \frac{\mu_i V_{th}}{|z_i|} & i = 1, \dots, M \\
(1d) \quad & \operatorname{div} \mathbf{E} = \frac{\rho}{\varepsilon} \\
(1e) \quad & \mathbf{E} = -\nabla \varphi \\
(1f) \quad & \rho = q \sum_{i=1}^M z_i c_i + qP.
\end{aligned}$$

In the PNP system, (1a) is the continuity equation describing mass conservation for each ion whose concentration is denoted by c_i (m^{-3}), $i = 1, \dots, M$, $M \geq 1$ being the number of ions flowing in the electrolyte fluid. Each ion flux density \mathbf{f}_i ($\text{m}^{-2}\text{s}^{-1}$) is defined by the Nernst-Planck relation (1b) in which it is possible to recognize a chemical contribution and an electric contribution, in such a way that the model be regarded as an extension of Fick's law of diffusion to the case where the diffusing particles are also moved by electrostatic forces with respect to the fluid. The quantity z_i is the valence of the i -th ion, while μ_i and D_i are the mobility and diffusivity of the chemical species, respectively, related by the Einstein relation (1c) where $V_{th} = k_B T_{sys}/q$ (V) is the thermal potential, our having denoted by k_B , T_{sys} and q , the Boltzmann constant, the absolute temperature of the system and the elementary charge, respectively. We remark that in the PNP modeling approach, T_{sys} is a parameter representing the constant temperature of the system, without distinction between the ionic species and the electrolyte fluid. This assumption is going to be relaxed in Section 4. The function ρ is the space charge density (Cm^{-3}) in the electrolyte and is given by the sum of two contributions, the mobile ion charge $q \sum_{i=1}^M z_i c_i$ and the fixed charge qP . The electric field \mathbf{E} (Vm^{-1}) due to space charge distribution ρ in the electrolyte is determined by the Poisson equation (1d) which represents Gauss' law in differential form, ε being the dielectric permittivity of the electrolyte fluid medium. For further development, it is useful to introduce the electrical current density \mathbf{j}_i (Am^{-2}), equal to the number of ion charges flowing through a given surface area per unit time and defined as

$$(1g) \quad \mathbf{j}_i := q z_i \mathbf{f}_i = -q z_i D_i \nabla c_i + q \mu_i |z_i| c_i \mathbf{E} \quad i = 1, \dots, M.$$

Remark 1. *The PNP system (1) has the same format and structure as the Drift-Diffusion (DD) equations for semiconductors (see, e.g., [18]), but it is applied to a different medium (water instead of a semiconductor crystal lattice) and includes, in general, more charge carriers than just holes and electrons, as in the case of semiconductor device theory.*

3. GEOMETRY, BIOPHYSICAL ASSUMPTIONS AND BOUNDARY CONDITIONS

Following the presentation of [9], we illustrate in Fig. 1 the schematic representation of a cross-section of a biological channel, assuming rotational invariance around the channel axis (x axis).

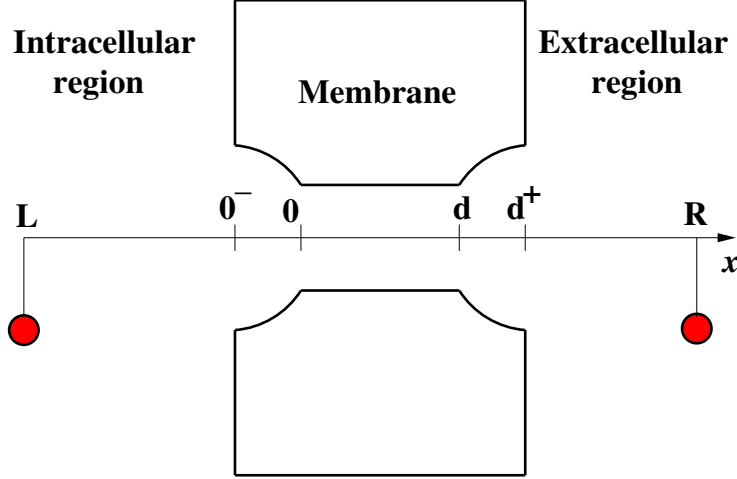


FIGURE 1. Schematic view of the biophysical problem. Five regions can be distinguished. From left to right: intracellular bathing solution, antichamber, channel region, antichamber, bathing solution in the extracellular side. At the endpoints, $x = 0$ and $x = L$, terminal contacts are marked in red color.

Five regions can be distinguished, ordered from left to right:

- (1) Region 1, $L \leq x \leq 0^-$: this is the bathing solution in the intracellular side.
- (2) Region 2, $0^- < x \leq 0$: this is the channel antichamber (or access region) from the intracellular side.
- (3) Region 3, $0 \leq x < d$: this is the channel region.
- (4) Region 4, $d \leq x < d^+$: this is the channel antichamber from the extracellular side.
- (5) Region 5, $d^+ \leq x \leq R$: this is the bathing solution in the extracellular side.

The above geometrical representation leads naturally to a multi-domain formulation for ion channel simulation. The biophysical treatment of such a problem is fully carried out in [9] whilst its mathematical and numerical treatment is the object of the present article, where the PNP formulation (1) is extended to include thermo-hydrodynamical phenomena to ion electrodiffusion in the channel.

3.1. Assumptions. The endpoints of the domain, $x = L$ and $x = R$, are located sufficiently far from the antichamber and channel regions, in such a way that appropriate equilibrium conditions can be applied. More importantly, the endpoints are assumed to be the physical place where the solution intra and extra-cellular electrochemical conditions are accessible to experimental measurements. Because of this, following [8, 9], we assume that at $x = L$ and $x = R$:

(A1): the electric potential φ is a known given quantity, so that:

$$(2a) \quad \varphi(L) = \varphi_L$$

$$(2b) \quad \varphi(R) = \varphi_R;$$

(A2): the ion concentrations c_i are known given quantities, so that:

$$(2c) \quad c_i(L) = c_{i,L}, \quad i = 1, \dots, M$$

$$(2d) \quad c_i(R) = c_{i,R}, \quad i = 1, \dots, M$$

where $M \geq 1$ is the number of ions flowing in the cellular solution. The boundary values for the ion concentrations satisfy the electroneutrality constraint:

$$(2e) \quad \sum_{i=1}^M z_i c_{i,L} = 0$$

$$(2f) \quad \sum_{i=1}^M z_i c_{i,R} = 0$$

where z_i is the charge number associated with each ion species c_i ($z_i > 0$ for cations, $z_i < 0$ for anions and $z_i = 0$ for neutral species).

We close the characterization of the bathing regions by assuming that:

(A3): the ion flux densities vanish inside the baths

$$(2g) \quad J_i(x) = 0 \quad L \leq x \leq 0^-, \quad i = 1, \dots, M$$

$$(2h) \quad J_i(x) = 0 \quad d^+ \leq x \leq R, \quad i = 1, \dots, M.$$

Continuing to move from the periphery of the domain towards the channel region, we encounter the antichamber openings, at $x = 0^-$ and $x = d^+$, respectively. Located on the membrane lipid bilayer, a space-dependent fixed charge density $P = P(x)$ is distributed. We make the following assumptions within the antichamber regions:

(A4): electroneutrality holds at the channel mouth entrances:

$$(2i) \quad qP(0^-) + q \sum z_j c_j(0^-) = 0$$

$$(2j) \quad qP(d^+) + q \sum z_j c_j(d^+) = 0;$$

(A5): the electric potential is constant in the antichamber regions:

$$(2k) \quad \varphi(x) = \varphi(0^-) \quad 0^- \leq x \leq 0$$

$$(2l) \quad \varphi(x) = \varphi(d^+) \quad d^- \leq x \leq d^+;$$

(A6): the ion concentrations are constant in the antichamber regions:

$$(2m) \quad c_i(x) = c_i(0^-) \quad 0^- \leq x \leq 0 \quad i = 1, \dots, M$$

$$(2n) \quad c_i(x) = c_i(d^+) \quad d \leq x \leq d^+ \quad i = 1, \dots, M.$$

3.2. Boundary Conditions at Channel Openings. In this section we use the geometrical multi-domain representation of the problem of Sect. 3 and the assumptions made in Sect. 3.1 to derive the boundary conditions to be supplied to the PNP Model at $x = 0$ and $x = d$ (channel openings). Using Einstein's relation (1c) in (1g) we can write the PNP current density as

$$(3a) \quad J_i = -q|z_i|\mu_i c_i \frac{\partial \varphi_i^{ec}}{\partial x} \quad i = 1, \dots, M$$

where

$$(3b) \quad \varphi_i^{ec} := \varphi + \frac{1}{z_i} V_{th} \ln \left(\frac{c_i}{c_{ref}} \right) \quad i = 1, \dots, M$$

is the electrochemical potential and $c_{ref} := \max_{i=1, \dots, M} \{c_{i,L}; c_{i,R}\}$ is a reference concentration. Inverting (3b) we obtain the well-known Maxwell-Boltzmann (MB) statistics for the ion densities

$$(3c) \quad c_i = c_{ref} \exp \left(z_i \frac{\varphi_i^{ec} - \varphi}{V_{th}} \right) \quad i = 1, \dots, M.$$

Using (A3) we get

$$(3d) \quad \varphi_i^{ec}(x) = const =: \overline{\varphi_{i,L}^{ec}} \quad L \leq x \leq 0^- \quad i = 1, \dots, M$$

$$(3e) \quad \varphi_i^{ec}(x) = const =: \overline{\varphi_{i,R}^{ec}} \quad d^+ \leq x \leq R \quad i = 1, \dots, M$$

where $\overline{\varphi_{i,L}^{ec}}$ and $\overline{\varphi_{i,R}^{ec}}$, $i = 1, \dots, M$, are constants yet to be determined. From (3c) we get

$$(3f) \quad c_i(x) = c_{ref} \exp \left(z_i \frac{(\varphi_i^{ec}(x) - \varphi(x))}{V_{th}} \right) \quad L \leq x \leq R \quad i = 1, \dots, M.$$

Thus, using (3d) and (3e) and assumptions (A5) and (A6), we find:

$$c_i(x) = c_{ref} \exp \left(z_i \frac{(\overline{\varphi_{i,L}^{ec}} - \varphi(x))}{V_{th}} \right) \quad L \leq x \leq 0 \quad i = 1, \dots, M$$

$$c_i(x) = c_{ref} \exp \left(z_i \frac{(\overline{\varphi_{i,R}^{ec}} - \varphi(x))}{V_{th}} \right) \quad d \leq x \leq R \quad i = 1, \dots, M.$$

Using (A2) in the equations above at $z = L$ and $z = R$, respectively, we obtain the boundary values for the electrochemical potential:

$$(3g) \quad \overline{\varphi_{i,L}^{ec}} = \varphi_L + \frac{V_{th}}{z_i} \ln \left(\frac{c_{i,L}}{c_{ref}} \right) \quad i = 1, \dots, M$$

$$(3h) \quad \overline{\varphi_{i,R}^{ec}} = \varphi_R + \frac{V_{th}}{z_i} \ln \left(\frac{c_{i,R}}{c_{ref}} \right) \quad i = 1, \dots, M.$$

Remark 2. It is important to note that relations (3g) and (3h) allow one to express the electrochemical potentials at the contacts as a function of the sole accessible quantities. This is in contrast with [24], page 42, relations (3.8a)-(3.8b), where the values of the electrochemical potentials were imposed and the corresponding values of the electrical potential were computed using (3.14a)-(3.14b).

From the previous discussion, we see that electroneutrality holds at the external contacts ($x = L$, $x = R$) and at the channel mouth entrances ($x = 0^-$, $x = d^+$), but not, in general, elsewhere. Therefore, it makes sense to introduce the voltage drops occurring in the bathing solution regions, the so-called built-in potentials:

$$(4a) \quad \varphi_{bi}(0^-) := \varphi(L) - \varphi(0^-)$$

$$(4b) \quad \varphi_{bi}(d^+) := \varphi(d^+) - \varphi(R).$$

Using the charge neutrality conditions (2i) and (2j), the MB relations (3c) and the definitions (4), the built-in potentials can be determined by solving the two following nonlinear algebraic equations:

$$(4c) \quad P(0^-) + \sum_{i=1}^M z_i c_{i,L} \exp\left(z_i \frac{\varphi_{bi}(0^-)}{V_{th}}\right) = 0$$

$$(4d) \quad P(d^+) + \sum_{i=1}^M z_i c_{i,R} \exp\left(-z_i \frac{\varphi_{bi}(d^+)}{V_{th}}\right) = 0.$$

Remark 3. *In the particular case of the KCl solution ($z_1 = +1$, $z_2 = -1$) considered in [8], equations (4c) and (4d) can be explicitly solved, to yield:*

$$\begin{aligned} \varphi_{bi}(0^-) &= V_{th} \ln \left(\frac{-P(0^-) + \sqrt{(P(0^-))^2 + 4(c_{1,L})^2}}{2c_{1,L}} \right) \\ \varphi_{bi}(d^+) &= V_{th} \ln \left(\frac{P(d^+) + \sqrt{(P(d^+))^2 + 4(c_{1,R})^2}}{2c_{1,R}} \right) \end{aligned}$$

where we notice that $c_{1,L} = c_{2,L}$ and $c_{1,R} = c_{2,R}$ because of the electroneutrality constraints (2e) and (2f).

In order to complete the characterization of the boundary values for the dependent variables of the problem we need the value of the electric potential and of the ion concentrations at the two endpoints of the channel. The potential is determined using (4) and (A5), which yield:

$$(5a) \quad \varphi(0) = \varphi(0^-) = \varphi_L - \varphi_{bi}(0^-)$$

$$(5b) \quad \varphi(d) = \varphi(d^+) = \varphi_R + \varphi_{bi}(d^+).$$

To determine the ion concentrations we use (3f), (3g) and (4a) at $x = 0$ to obtain

$$(5c) \quad c_i(0) = c_{ref} \exp\left(z_i \frac{(\varphi_i^{ec}(0) - \varphi(0))}{V_{th}}\right) = c_{i,L} \exp\left(z_i \frac{\varphi_{bi}(0^-)}{V_{th}}\right) \quad i = 1, \dots, M$$

and (3f), (3h) and (4b) at $x = d$ to obtain

$$(5d) \quad c_i(d) = c_{ref} \exp\left(z_i \frac{(\varphi_i^{ec}(d) - \varphi(d))}{V_{th}}\right) = c_{i,R} \exp\left(-z_i \frac{\varphi_{bi}(d^+)}{V_{th}}\right) \quad i = 1, \dots, M.$$

Summarizing, the Dirichlet boundary conditions for the PNP system in the reduced channel domain $\Omega = (0, d)$ are at $x = 0$:

$$(6a) \quad P(0^-) + \sum_{i=1}^M z_i c_{i,L} \exp\left(z_i \frac{\varphi_{bi}(0^-)}{V_{th}}\right) = 0$$

$$(6b) \quad \varphi(0) = \varphi_L - \varphi_{bi}(0^-)$$

$$(6c) \quad \varphi_i^{ec}(0) = \varphi_L + \frac{1}{z_i} V_{th} \ln\left(\frac{c_{i,L}}{c_{ref}}\right) \quad i = 1, \dots, M$$

$$(6d) \quad c_i(0) = c_{i,L} \exp\left(z_i \frac{\varphi_{bi}(0^-)}{V_{th}}\right) \quad i = 1, \dots, M$$

and, at $x = d$:

$$(6e) \quad P(d^+) + \sum_{i=1}^M z_i c_{i,R} \exp\left(z_i \frac{\varphi_{bi}(d^+)}{V_{th}}\right) = 0$$

$$(6f) \quad \varphi(d) = \varphi_R + \varphi_{bi}(d^+)$$

$$(6g) \quad \varphi_i^{ec}(d) = \varphi_R + \frac{1}{z_i} V_{th} \ln\left(\frac{c_{i,R}}{c_{ref}}\right) \quad i = 1, \dots, M$$

$$(6h) \quad c_i(d) = c_{i,R} \exp\left(-z_i \frac{\varphi_{bi}(d^+)}{V_{th}}\right) \quad i = 1, \dots, M.$$

4. EXTENSIONS OF THE PNP MODEL

In this section we present two extensions of the PNP equation system illustrated in Sections 2 and 3. From now on we restrict our attention to the study of a channel in stationary conditions and to simplify the exposition, in close analogy with semiconductor device physics, we consider a binary mixture of *monovalent* anions and cations, i.e., such that their chemical valence is equal to ± 1 as in the case of the *KCl* solution or the *NaCl* solution. We use the symbol p (positive) and n (negative) to refer to the concentrations of cations and anions, respectively. The symbol ν is used to indicate either p or n . When the operators \mp or \pm are used, the upper sign always refers to n -type particles, the lower sign to p -type particles, and the value for ν must be chosen accordingly. The quantities associated with the electrolyte medium are referred to by the symbol e , while x denotes henceforth the spatial coordinate.

In our analysis we follow [24], the series of references [18, 4, 32] in the context of semiconductor device modeling, and the theory of [31, 19, 20, 35].

The first extension is denoted velocity-extended Thermo-Hydrodynamic model (vTHD) and the second extension is denoted velocity-extended Electro-Thermal model (vET). Both extensions include thermal driving forces and the translational contribution of electrolyte fluid flow, besides the usual electrochemical forces accounted for by the PNP equations. In the vTHD model the temperature of anions, cations and lattice are considered as distinct dependent variables, while in the vET model there is only one temperature, generally varying with the spatial coordinate x , to describe the global system.

Finally, in the present article we assume the electrolyte fluid velocity v_e to be a given function of x . This is a strong simplification which is going to be removed in a future publication. Moreover, to self-consistently account for electrodynamical effects, we adjoin to both vTHD and vET model the solution of the Poisson equation, written below in conservation form:

$$(7a) \quad \frac{\partial E}{\partial x} = \frac{q}{\epsilon}(p - n + P)$$

$$(7b) \quad E = -\frac{\partial \varphi}{\partial x}.$$

4.1. Thermodynamical Equilibrium. Let $T_p = T_p(x)$, $T_n = T_n(x)$ and $T_e = T_e(x)$ denote the temperatures of cations, anions and electrolyte, respectively, with $x \in [0, d]$. Let also T_{sys} be a given value representing the constant temperature of the whole environment (ions + fluid). By definition, thermal equilibrium is the condition corresponding to applying no external electrical, mechanical, chemical and thermal

forces to the biophysical system. In such a case, system response is represented by the following values of the dependent variables:

$$\begin{aligned} (8a) \quad & v_\nu(x) = 0 \\ (8b) \quad & v_e(x) = 0 \\ (8c) \quad & T_p(x) = T_n(x) = T_e(x) = T_{sys}. \end{aligned}$$

Eq. (8a) expresses the fact that the ion drift velocity is equal to zero, while Eq. (8b) expresses the fact that the fluid translational velocity is equal to zero. Eq. (8c) expresses the fact that the system settles in an isothermal condition. The three above conditions imply that:

$$\begin{aligned} (8d) \quad & J_\nu(x) = 0 \\ (8e) \quad & S_\nu(x) = S_e(x) = 0 \end{aligned}$$

where J_p and J_n are anion and cation current flows, while S_ν and S_e are ion and fluid energy fluxes. Using (3a) in (8d) tells us that at thermal equilibrium each ion electrochemical potential is constant in $[0, d]$

$$(8f) \quad \varphi_\nu^{ec}(x) = \varphi_{\nu,eq}^{ec}$$

where the constant value $\varphi_{\nu,eq}^{ec}$ is different for each ion and can be computed as detailed in Sect. 3.2. Model consistency requires that under thermal equilibrium any extension of the PNP system verifies all conditions (8). This fact is documented in the later sections where the vTHD and vET models are introduced.

4.2. Velocity-extended Thermo-Hydrodynamic (vTHD) model. The stationary velocity-extended thermo-hydrodynamic model in the one-dimensional setting consists of the following system of conservation laws (see [36, Chap. 2] and [18, 4, 32]):

$$\begin{aligned} (9a) \quad & \frac{1}{q} \frac{\partial J_\nu}{\partial x} = 0 \\ (9b) \quad & J_\nu + \nu \tau_{p_\nu} v_\nu \frac{\partial}{\partial x} \left(\frac{J_\nu}{\nu} \right) = \pm q D_\nu \frac{\partial \nu}{\partial x} - q \mu_\nu \nu \frac{\partial}{\partial x} \left(\varphi \mp \frac{k_B T_\nu}{q} \right) \mp q \nu v_e \\ (9c) \quad & \frac{\partial S_\nu}{\partial x} = E J_\nu - \frac{\nu}{\tau_{w_\nu}} (w_\nu - w_\nu^{eq}) \\ (9d) \quad & \frac{\partial S_e}{\partial x} = \left[\frac{p}{\tau_{w_p}} (w_p - w_p^{eq}) + \frac{n}{\tau_{w_n}} (w_n - w_n^{eq}) \right] \\ (9e) \quad & S_\nu = -\kappa_\nu \frac{\partial T_\nu}{\partial x} \mp \frac{J_\nu}{q} (w_\nu + k_B T_\nu) \\ (9f) \quad & S_e = -\kappa_e \frac{\partial T_e}{\partial x} + N_e v_e w_e \\ (9g) \quad & w_\nu = \frac{1}{2} m_\nu |v_\nu|^2 + \frac{3}{2} k_B T_\nu \\ (9h) \quad & w_e = \frac{1}{2} m_e |v_e|^2 + \frac{3}{2} k_B T_e \\ (9i) \quad & w_\nu^{eq} = \frac{3}{2} k_B T_e. \end{aligned}$$

In system (9), ν and T_ν represent ion density and temperature, N_e and T_e are electrolyte number density and temperature, while v_ν , J_ν , S_ν and S_e represent the drift (or translational) velocity of each ion, the ion current density, the ion energy density flux and the electrolyte energy density flux, respectively. The drift velocities and the current densities are related through the phenomenological law

$$(10a) \quad v_\nu = \mp \frac{J_\nu}{q \nu}$$

Eq. (9a) expresses conservation of ion density, eq. (9b) expresses conservation of ion momentum density, eqns. (9c) and (9d) express conservation of the energy densities for ions and electrolyte fluid, eqns. (9e) and (9f) are constitutive laws for ion and electrolyte energy density fluxes S_ν and S_e , respectively.

The quantities κ_ν and κ_e are the thermoconductivity coefficients of ions and electrolyte, respectively, while τ_{p_ν} and τ_{w_ν} are the momentum and energy relaxation times, respectively. Phenomenological expressions for these coefficients are:

$$(11a) \quad \tau_{p_\nu} = \frac{m_\nu \mu_{0\nu} T_e}{q T_\nu},$$

$$(11b) \quad \tau_{w_\nu} = \frac{3}{2} \frac{\mu_{0\nu} k_B T_\nu T_e}{q v_{sat}^2 (T_\nu + T_e)} + \frac{\tau_{p_\nu}}{2},$$

$$(11c) \quad \kappa_\nu = \frac{3}{2} \frac{\mu_{0\nu} k_B^2 T_e}{q} \nu,$$

where $\mu_{0\nu}$ is the low-field mobility and v_{sat} is the saturation velocity. For a physical interpretation of the parameter v_{sat} and its influence on system behavior, we refer to [10, 24].

The ion mobility

$$(12a) \quad \mu_\nu = \frac{q}{m_\nu} \tau_{p_\nu}$$

is related to the diffusion coefficient D_ν by the generalized Einstein relation

$$(12b) \quad D_\nu = \mu_\nu \frac{k_B T_\nu}{q} = \frac{k_B T_\nu}{m_\nu} \tau_{p_\nu}$$

where m_ν is the ionic mass.

Finally, w_ν and w_e are the ion and electrolyte energies, in which we can distinguish a kinetic contribution and a thermal contribution. The quantities w_p^{eq} and w_n^{eq} are the equilibrium energies of cations and anions.

Proposition 1 (Consistency with respect to thermal equilibrium). *The vTHD satisfies relations (8).*

Proof. Using (8a), (8b) and (8c) in (9b) and (12b) we get

$$J_\nu = \pm q \mu_\nu \frac{k_B T_{sys}}{q} \frac{\partial \nu}{\partial x} - q \mu_\nu \nu \frac{\partial \varphi}{\partial x} = 0$$

or, equivalently,

$$J_\nu = -q \mu_\nu \nu \frac{\partial}{\partial x} (\mp V_{th} \ln(\nu/\nu_{ref}) + \varphi) = 0.$$

The above equation represents the particle flux equilibrium condition (8d) and can be written in the form (3a) upon defining the equilibrium electrochemical potential

$$\varphi_\nu^{ec} := \varphi \mp V_{th} \ln \left(\frac{\nu}{\nu_{ref}} \right)$$

which corresponds to (3b) having set $z_n = -1$ and $z_p = +1$. Having proved (8d) (and, equivalently, (8f)) and using (8c) in (9e) and (9f), we immediately obtain

$$S_n = S_p = S_e = 0$$

that is the energy flux equilibrium condition (8e). We notice that at thermal equilibrium the ion and fluid energies coincide with their rest energy

$$w_n = w_p = w_e = \frac{3}{2} k_B T_{sys}.$$

□

4.3. Velocity-extended Electro-Thermal (vET) model. This model differs quite significantly from the vTHD because of the following simplifying assumptions:

(H1): cations, anions and electrolyte are in local equilibrium, i.e.

$$(13a) \quad T_n = T_p = T_e =: T(x).$$

This situation occurs when the system is assumed to have had enough time to evolve and to reach steady state;

(H2): the kinetic energy is small compared to the thermal energy, i.e.

$$(13b) \quad \frac{1}{2} m_\nu |v_\nu|^2 \ll \frac{3}{2} k_B T.$$

Thus we can write

$$(13c) \quad w_\nu \simeq \frac{3}{2} k_B T$$

and neglect the nonlinear inertial term in the momentum balance equation (9b).

Using (H1), and summing up the three resulting energy balance equations we obtain the following equations of the velocity-extended ET system:

$$(14a) \quad \frac{1}{q} \operatorname{div} J_\nu = 0$$

$$(14b) \quad J_\nu = q \mu_\nu \nu E \pm \mu_\nu \frac{\partial}{\partial x} (\nu k_B T) \mp q \nu v_e$$

$$(14c) \quad \operatorname{div} S_{tot} = E \cdot (J_n + J_p) - \operatorname{div} \left(\frac{5}{2} \frac{k_B T}{q} (J_p - J_n) \right)$$

$$(14d) \quad S_{tot} = \left(-\kappa_{tot} \frac{\partial T}{\partial x} + \frac{3}{2} k_B T N_e v_e \right)$$

$$(14e) \quad \kappa_{tot} = \kappa_e + \kappa_n + \kappa_p.$$

Remark 4. Looking at the (simplified) momentum conservation equation (14b), we see that it now furnishes an explicit expression for the current density as a function of concentration, electric potential and temperature. This allows one to adopt the basic ideas of the Scharfetter-Gummel discretization method [34], which is the most

widely used numerical scheme in contemporary semiconductor device simulation because of its remarkable stability and accuracy.

Remark 5. Simple manipulations of (14b) show that it can be written in the following equivalent DD form

$$(14f) \quad J_\nu = \pm q D_\nu \frac{\partial \nu}{\partial x} + q \mu_\nu \nu E_\nu$$

where

$$(14g) \quad E_\nu = E \mp \frac{v_e}{\mu_\nu} \pm \frac{\partial}{\partial x} \left(\frac{k_B T}{q} \right).$$

The effective electric drift E_ν acting on each ion species can be interpreted as the linear superposition of the electric, fluid and thermal forces that drive ion motion in the electrolyte channel fluid. Relation (14f) can be interpreted as the formal limit of (9b) as the relaxation time $\tau_{p_\nu} \rightarrow 0$.

Proposition 2 (Consistency with respect to thermal equilibrium). *The vET satisfies relations (8).*

Proof. The proof is similar to that for the vTHD model and therefore it is omitted. \square

5. SOLUTION MAP FOR THE vTHD SYSTEM

In this section we describe the solution map that is used to iteratively solve the vTHD and vET models. The description of the method is discussed in detail in the case of the vTHD system as a similar approach is used to treat also the vET model. The adopted solution map is an extension of the decoupled algorithm known as Gummel's map, a functional tool widely employed in contemporary Drift-Diffusion simulation of semiconductor devices [18, 36, 26]. The Gummel solution map is basically a nonlinear block Gauss-Seidel iteration that allows one to subdivide the considered PDE model system into blocks of single equations to be solved separately and in sequence until convergence is achieved.

To describe the method, we follow the idea proposed in [1] (cf. Eq. (25) of this latter reference), and we introduce the generalization of the Maxwell-Boltzmann statistics (3c) to the case of the vTHD system:

$$(15a) \quad n = c_{ref} \exp \left(q \frac{\varphi - \varphi_n}{k_B T_n} \right)$$

$$(15b) \quad p = c_{ref} \exp \left(q \frac{\varphi_p - \varphi}{k_B T_p} \right)$$

where, for notational brevity, we have omitted the superscript ec in the electrochemical potentials for anions and cations. The main difference between the definitions (15) and the corresponding (3c) valid in the case of the standard PNP model, is that the ion temperatures T_n and T_p are used instead of the system (constant) temperature T_{sys} . Assuming local thermal equilibrium at the channel entrance and outlet, the temperature of the ions and of the fluid satisfy the following Dirichlet boundary conditions:

$$(16a) \quad T_n^0(0) = T_p^0(0) = T_e^0(0) = T_L$$

$$(16b) \quad T_n^0(d) = T_p^0(d) = T_e^0(d) = T_R.$$

We notice that T_L and T_R are the externally accessible temperatures of the intra and extracellular baths, not necessarily being equal to the same value. This feature of the model is important when an external temperature gradient has to be enforced across the channel to model the heat biosensors described in Sect. 1. Conditions (16) imply that $V_{th} = k_B T_L / q$ at $x = 0$ and $V_{th} = k_B T_R / q$ at $x = d$.

The Gummel algorithm for the iterative solution of the vTHD model starts with an initial guess $[\varphi^0, \varphi_p^0, \varphi_n^0, T_p^0, T_n^0, T_e^0]^T$ that satisfies the boundary conditions (6) and (16). Then, for $k \geq 0$ until convergence, the algorithm consists of the following steps:

- (1) solve with the damped Newton method (see [36], Chapt. 7) the nonlinear Poisson equation (NLP) resulting from substituting (15) into (7). This returns the updated potential φ^{k+1} ;
- (2) solve the continuity and momentum balance equations (9a)- (9b). This returns the updated concentrations p^{k+1}, n^{k+1} ;
- (3) solve the energy equations (9c)- (9e) . This returns the updated ion temperatures T_p^{k+1}, T_n^{k+1} ;
- (4) solve the fluid energy equation (9d)- (9f). This returns the updated fluid temperature T_e^{k+1} ;
- (5) update the electrochemical potentials by inverting (15):

$$(17a) \quad \varphi_n^{k+1} = \varphi^{k+1} - \frac{k_B T_n^{k+1}}{q} \ln \left(\frac{n^{k+1}}{c_{ref}} \right)$$

$$(17b) \quad \varphi_p^{k+1} = \varphi^{k+1} + \frac{k_B T_p^{k+1}}{q} \ln \left(\frac{p^{k+1}}{c_{ref}} \right);$$

- (6) check the convergence of the iteration by controlling whether the maximum absolute difference between two consecutive iterations k and $k + 1$ is less than a prescribed tolerance

$$(17c) \quad \max_{\eta \in U} \|\eta^{k+1} - \eta^k\|_\infty < \mathbf{toll}$$

where \mathbf{toll} is a given tolerance, U is the set of unknowns $[\varphi, \varphi_p, \varphi_n, T_p, T_n, T_e]^T$ and $\|\cdot\|_\infty$ is the L^∞ norm. If condition (17c) is satisfied, the algorithm stops.

A deep analysis of the convergence properties and mathematical foundations of the Gummel decoupling algorithm for the stationary DD model of semiconductors can be found in [18]. Preconditioning strategies for improving the convergence rate of the map are investigated in [23].

6. THE ADVECTION-DIFFUSION-REACTION MODEL PROBLEM

As outlined in items (e)-(h) of the introduction, we are providing a detailed description of the algorithm, beginning in this section, and continuing through Section 9.

All the linearized equations of the vTHD system (9) that need be solved during the iterative procedure described in Sect. 5 can be cast into the following general Boundary Value model Problem (BVP):

find u and J such that:

$$(18a) \quad \frac{\partial J}{\partial x} + cu = g \quad \text{in } \Omega$$

$$(18b) \quad J = vu - D \frac{\partial u}{\partial x} \quad \text{in } \Omega$$

$$(18c) \quad u = \bar{u} \quad \text{on } \partial\Omega.$$

In (18), Ω is the open interval $(0, d)$, u and J denote the primal unknown and the associated flux, while c and g are the reaction and production terms such that (18a) can be regarded as a stationary conservation law for u . In view of the numerical treatment of (18) we assume D , v , c and g to be piecewise smooth functions in Ω , the diffusion coefficient D being a positive bounded function while c and g are nonnegative given functions. Dirichlet boundary conditions are expressed by the nonnegative function $\bar{u} : \partial\Omega \rightarrow \mathbb{R}^+$. Let

$$(19a) \quad \mathcal{L}u := \frac{\partial J}{\partial x} + cu = \frac{\partial}{\partial x} \left(-D \frac{\partial u}{\partial x} + vu \right) + cu : \Omega \rightarrow \mathbb{R}.$$

The following properties express important biophysical features of the solution of the linearized BVP (18). We refer the reader to [30] for details and examples.

Definition 1 (Inverse monotonicity). *Let $w \in C^2(\Omega) \cap C^0(\bar{\Omega})$. We say that \mathcal{L} is inverse-monotone if the inequalities*

$$(19b) \quad \mathcal{L}w(x) \geq 0 \quad \forall x \in \Omega$$

$$(19c) \quad w(x) \geq 0 \quad \forall x \in \partial\Omega$$

together imply that

$$(19d) \quad w(x) \geq 0 \quad \forall x \in \bar{\Omega}.$$

Remark 6. *Inverse monotonicity expresses the fact that the dependent variable of the problem, say, a concentration, a temperature or a mass density, cannot take negative values.*

Theorem 1 (Comparison principle). *Suppose that there exists a function $\phi \in C^2(\Omega) \cap C^0(\bar{\Omega})$ such that*

$$(19e) \quad \mathcal{L}u(x) \leq \mathcal{L}\phi(x) \quad \forall x \in \Omega$$

$$(19f) \quad u(x) \leq \phi(x) \quad \forall x \in \partial\Omega.$$

Then, we have

$$(19g) \quad u(x) \leq \phi(x) \quad \forall x \in \Omega$$

and we say that ϕ is a barrier function for u .

Combining (19d) and (19g), we obtain the following result which is a very useful tool in the approximation process of the BVP (18).

Theorem 2 (Continuous Maximum Principle). *Suppose that \mathcal{L} is inverse-monotone and that the comparison principle holds for a suitable barrier function ϕ . Then, setting $M_\phi := \max_{x \in \Omega} \phi(x)$, we have*

$$(19h) \quad 0 \leq u(x) \leq M_\phi \quad \forall x \in \bar{\Omega}$$

and we say that u satisfies a continuous maximum principle (CMP).

7. FINITE ELEMENT APPROXIMATION

The content of the present methodological section is organized as follows. In Sect. 7.1 we introduce the dual-mixed weak formulation of (18) and in Sect. 7.2 its corresponding hybridized finite element approximation, denoted DMH method. Then, in Sections 7.3 and 7.4 we illustrate how to reduce the computational complexity of the dual-mixed hybridized method by the use of static condensation, which leads to solving a linear algebraic system of the same structure as a standard nodal-based finite element scheme.

7.1. Continuous formulation. In the dual mixed method, the variables u and J in (18) are treated as independent unknowns, each of which belongs to a different functional space, namely $u \in V := L^2(\Omega)$ and $J \in Q := H(\operatorname{div}, \Omega) \equiv H^1(\Omega)$. We proceed by formally multiplying equation (18a) by a test function $w \in V$ and equation (18b) by a test function $q \in Q$, and integrate by parts over Ω to obtain the problem:

find $(u, J) \in V \times Q$ such that, for all $(w, q) \in V \times Q$:

$$\begin{aligned} (20a) \quad & \left\{ \int_{\Omega} D^{-1}(J - vu) q \, dx - \int_{\Omega} u \frac{\partial q}{\partial x} \, dx = - \int_{\partial\Omega} (q \cdot \mathbf{n}) \bar{u} \, d\sigma \right. \\ (20b) \quad & \left. - \int_{\Omega} \frac{\partial J}{\partial x} w \, dx - \int_{\Omega} cuw \, dx = - \int_{\Omega} gw \, dx. \right. \end{aligned}$$

Existence and uniqueness of the solution pair (u, J) of problem (20) can be proved under suitable coercivity assumptions, see [11].

7.2. Discrete formulation. We denote by Ω the open interval $(0, L)$ and by $\partial\Omega = \{0, L\}$ its boundary on which an outward unit normal \mathbf{n} is defined, in such a way that $\mathbf{n}(0) = -1$ and $\mathbf{n}(L) = +1$. We introduce a partition (triangulation) \mathcal{T}_h of $\bar{\Omega}$ into a number $N_{el} \geq 2$ of intervals $K_i = [x_i, x_{i+1}]$, $i = 1, \dots, N_{el}$, with $x_1 = 0$ and $x_{N_{el}+1} = L$. On each element K_i we introduce a local unit outward normal vector $\mathbf{n}|_{\partial K_i}$, we denote by $h_i := x_{i+1} - x_i$ the length of the interval and set $h := \max_{\mathcal{T}_h} h_i$. We also set $N := N_{el} + 1$ and denote with $\mathcal{N}_h := \{x_i\}_{i=1}^N$ the set of vertices of \mathcal{T}_h . We associate with \mathcal{T}_h the following function spaces:

$$\begin{aligned} (21a) \quad & V_h := \{w_h \in L^2(\Omega) \text{ s.t. } w_h|_K \in \mathbb{P}_0(K) \forall K \in \mathcal{T}_h\} \\ (21b) \quad & Q_h := \{q_h \in L^2(\Omega) \text{ s.t. } q_h|_K \in \mathbb{P}_1(K) \forall K \in \mathcal{T}_h\} \\ (21c) \quad & \Lambda_{h,\rho} := \{\lambda_h : \mathcal{N}_h \rightarrow \mathbb{R} \text{ s.t. } \lambda_h(a) = \rho_a, \lambda_h(b) = \rho_b\} \end{aligned}$$

where V_h is the vector space of piecewise constant polynomials defined over Ω , Q_h is the vector space of piecewise linear polynomials discontinuous over $\bar{\Omega}$, and $\Lambda_{h,\rho}$ is the space of functions defined only at the vertices of \mathcal{T}_h with given boundary values. Notice that $\dim(Q_h) = 2N_{el}$ because its functions are not continuous at interelement interfaces. The DMH formulation of problem (20) is:

find $(J_h, u_h, \lambda_h) \in Q_h \times V_h \times \Lambda_{h,\bar{u}}$ such that, for all $(q_h, w_h, \xi_h) \in Q_h \times V_h \times \Lambda_{h,0}$:

$$(22a) \quad \sum_{K \in \mathcal{T}_h} \left[\int_K D_h^{-1} (J_h - v u_h) q_h dx - \int_K u_h \frac{\partial q_h}{\partial x} dx + \int_{\partial K} (q_h \cdot \mathbf{n}|_{\partial K}) \lambda_h dx \right] = 0$$

$$(22b) \quad - \sum_{K \in \mathcal{T}_h} \left[\int_K \frac{\partial J_h}{\partial x} w_h dx - \int_K c u_h w_h dx \right] = - \sum_{K \in \mathcal{T}_h} \int_K g w_h dx$$

$$(22c) \quad \sum_{K \in \mathcal{T}_h} \int_{\partial K} (J_h \cdot \mathbf{n}|_{\partial K}) \xi_h dx = 0$$

where $D_h : \mathcal{T}_h \rightarrow \mathbb{R}^+$ is a modified diffusion coefficient containing a stabilization term to deal with advective-dominated problems.

Remark 7. *The proof of existence and uniqueness of the solution (J_h, u_h, λ_h) of (22) is not an easy task because of the advective term. In what follows, we assume that such a solution always exists and we refer to [5, 29] for the general theoretical tools required in the analysis of (22) and to [2] for an example of such analysis in the case of mixed methods interpreted as nonconforming discretizations.*

Remark 8. *Conditions (22c) imply the continuity of J_h across interdomain boundaries.*

Remark 9. *The hybrid variable λ_h is the Lagrange multiplier associated with the continuity constraint of $J_h \cdot \mathbf{n}$ and it can be regarded as an approximation of u at the grid nodes:*

$$\lambda_h \simeq u|_{\mathcal{N}_h}.$$

7.3. Static condensation. Consider a generic element $K \in \mathcal{T}_h$. From (22a), we can compute $J_h|_K$ by inverting the local flux mass matrix as

$$(23a) \quad \mathbf{J}_K = -A_K^{-1} \left[(B_K^T + C_K) u_K + L_K \boldsymbol{\lambda}_K \right] \in \mathbb{R}^{2 \times 1}.$$

Substituting \mathbf{J}_K into (22b), we get $u_h|_K$

$$(23b) \quad u_K = H_K^{-1} \left[g_K + B_K A_K^{-1} L_K \boldsymbol{\lambda}_K \right] \in \mathbb{R}^{1 \times 1}$$

where

$$H_K := \left[-B_K A_K^{-1} (B_K^T + C_K) + E_K \right] \in \mathbb{R}^{1 \times 1}.$$

Now, using (23b) in (23a), we can express \mathbf{J}_K in terms of the sole hybrid variable $\boldsymbol{\lambda}_K$ and of g_K as

$$(23c) \quad \mathbf{J}_K = M_K \boldsymbol{\lambda}_K + \mathbf{b}_K$$

where

$$M_K := - \left[A_K^{-1} (B_K^T + C_K) H_K^{-1} B_K A_K^{-1} L_K^T + A_K^{-1} L_K \right] \in \mathbb{R}^{2 \times 2}$$

and

$$\mathbf{b}_K := \left[-A_K^{-1} (B_K^T + C_K) H_K^{-1} g_K \right] \in \mathbb{R}^{2 \times 1}.$$

The above procedure is well known as *static condensation* and corresponds to Gaussian elimination of the internal variables $J_h|_K$ and $u_h|_K$ in favor of $\lambda_h|_{\partial K}$ at the level of the element $K \in \mathcal{T}_h$ (see [3]).

7.4. The algebraic system. Enforcing the continuity of J_h at each internal node through (22c) yields the following $N_{el} - 1$ conditions

$$(24a) \quad J_2^{K_i-1}(\lambda_{i-1}, \lambda_i) = J_1^{K_i}(\lambda_i, \lambda_{i+1}) \quad i = 1, \dots, M-1$$

which can be written in the form of a linear *tridiagonal* algebraic system for $\boldsymbol{\lambda}$, i.e., for $i = 1, \dots, M-1$:

$$(24ba) \quad \begin{cases} M_{21}^{K_i} \lambda_{i-1} + (M_{22}^{K_i} - M_{11}^{K_{i+1}}) \lambda_i - M_{12}^{K_{i+1}} \lambda_{i+1} = b_1^{K_{i+1}} - b_2^{K_i} \\ \lambda_1 = \bar{u}_0, \quad \lambda_N = \bar{u}_L. \end{cases}$$

Equations (24b) constitute a linear system of the form

$$(24c) \quad \mathcal{M}\boldsymbol{\lambda} = \mathbf{f}$$

where the entries of the stiffness matrix $\mathcal{M} \in \mathbb{R}^{M-1 \times M-1}$ are defined as:

$$(24da) \quad \begin{cases} \mathcal{M}_{i,i-1} = M_{21}^{K_i} \\ \mathcal{M}_{i,i} = M_{22}^{K_i} - M_{11}^{K_{i+1}} \\ \mathcal{M}_{i,i+1} = -M_{12}^{K_{i+1}} \end{cases}$$

and the entries of the load vector $\mathbf{f} \in \mathbb{R}^{M-1}$ are $f_i = b_1^{K_{i+1}} - b_2^{K_i}$. The explicit expressions of these entries will be specified in Sect. 8.1.

8. THE STABILIZED DMH METHOD AND THE DISCRETE MAXIMUM PRINCIPLE

If the solution of a given boundary value problem satisfies a CMP, then a properly designed approximation should behave in the same way. A numerical scheme that does not generate spurious global extrema in the interior of the computational domain is said to satisfy a *discrete maximum principle* (DMP). We assume that the solution u of the BVP (18) satisfies the a priori estimate (19h) and we characterize the conditions under which the same estimate is satisfied also by the DMH approximation λ_h computed by solving the linear algebraic system (24c) associated with the problem.

The following definitions turn out to be useful.

Definition 2 (Inverse monotone matrix). *An invertible square matrix A of size n is said to be inverse monotone if*

$$(25a) \quad A^{-1} \geq 0$$

the inequality being understood in the element-wise sense.

A special class of monotone matrices is that introduced below.

Definition 3 (M-matrix). *An invertible square matrix A is an M-matrix if:*

- $A_{ij} \leq 0$ for $i \neq j$;
- A is inverse-monotone.

Given a function $\eta_h \in \Lambda_{h,\rho}$, for any given function $\rho : \partial\Omega \rightarrow \mathbb{R}$, we denote by ρ_h^* the piecewise linear continuous interpolate of η_h over \mathcal{T}_h .

Theorem 3 (Sufficient condition for DMP). *Assume that matrix \mathcal{M} is an M-matrix. Then λ_h^* satisfies the DMP, i.e.*

$$(25b) \quad 0 \leq \lambda_h^*(x) \leq M_\phi \quad \forall x \in \bar{\Omega}.$$

The following (necessary and sufficient) condition is useful to verify the property of being an M-matrix.

Theorem 4 (Discrete comparison principle). *Let A be an invertible matrix with non-positive off diagonal entries ($A_{ij} \leq 0$ for $i \neq j$). Then, A is an M-matrix if and only if there exists a positive vector \mathbf{e} such that $A\mathbf{e} \geq 0$ (in the component-wise sense), with at least one row index i^* such that $(A\mathbf{e})_{i^*} > 0$.*

8.1. The stabilized DMH method. The solution of the model BVP (18) may exhibit sharp boundary and/or internal layers according to the relative weight of the advective and reactive coefficients with respect to the diffusion term (see [30]). Correspondingly, this is well known to reflect into numerical instability (spurious unphysical oscillations) if the local mesh size h is not sufficiently small. However, a smaller value of h means a larger size of the linear algebraic system and thus an increased computational effort. To avoid this inconvenience, we introduce in the DMH formulation (22) two specific approaches that ensure numerical stability without necessarily resorting to a small value of h :

(S1): diagonal *lumping* of the local mass flux matrix A_K (for dominant reaction);

(S2): addition of an *artificial diffusion* (for dominant convection).

In particular, in the remainder of the section we show that, when (S1) and (S2) are used in conjunction, the stiffness matrix \mathcal{M} is an M-matrix irrespective of the value of h . This property guarantees that system (24c) is uniquely solvable and that the piecewise linear interpolate of the solution, λ_h^* , satisfies the DMP and, in particular, the a-priori estimate (25b). We refer to [30] for a thorough discussion of continuous and discrete maximum principles enjoyed by the solution of singularly perturbed BVPs and by their corresponding finite element and finite difference approximations. For ease of presentation, we assume henceforth that problem coefficients D, v, c and g are constant positive quantities and that the mesh size is uniform and given by $h = 1/N_{el}$.

8.1.1. (S1): Lumping of the local flux mass matrix. The stabilization approach to deal with the case where the reaction coefficient c dominates over the diffusion coefficient D in (18) consists of replacing the local flux mass matrix A_K in (23a) with a diagonal matrix \hat{A}_K such that:

$$(26a) \quad (\hat{A}_K)_{ii} = \sum_{j=1}^2 (A_K)_{ij} = \frac{1}{2} \quad i = 1, 2$$

$$(26b) \quad (\hat{A}_K)_{ij} = 0 \quad i \neq j.$$

The approach (26) is referred to as *mass lumping* and is equivalent to using the trapezoidal quadrature rule to compute the integral

$$(A_K)_{ij} = \int_K \psi_j \psi_i dx \quad i, j = 1, 2$$

where

$$\mathbb{P}_1(K) = \text{span} \{\psi_1, \psi_2\} \quad \forall K \in \mathcal{T}_h.$$

Using (26) in (22a), when $q_h = \psi_1$, we get

$$(26c) \quad J_1 = vu_K - D_h \frac{u_K - \lambda_1}{h/2},$$

while, when $q_h = \psi_2$, we similarly get

$$(26d) \quad J_2 = vu_K - D_h \frac{\lambda_2 - u_K}{h/2}.$$

Equations (26c) and (26c) express each local degree of freedom of the flux $J_h|_K$ as the sum of an *average* advective flux and a finite difference approximation of the Fick diffusive flux flowing between the boundary of K and its center. The two relations are the DMH analogues of those of the dual-mixed stabilized method of [33].

8.1.2. *(S2): Artificial diffusion.* The stabilization approach to deal with the case where the advection coefficient v dominates over the diffusion coefficient D in (18) consists of replacing the diffusion coefficient D with the following modified expression (cf. [6])

$$(27a) \quad D_h := D(1 + \Phi(\mathcal{P}e_{loc}))$$

where $\mathcal{P}e_{loc} := \frac{|v|h}{2D}$ is the local Péclet number and $\Phi : \mathbb{R}^+ \rightarrow \mathbb{R}^+$ is a suitable stabilization function to be chosen in such a way that:

$$(27b) \quad \Phi(t) \geq 0$$

$$(27c) \quad \lim_{t \rightarrow 0^+} \Phi(t) = 0.$$

The approach (27a) is referred to as *artificial diffusion*. Two special choices of Φ are:

- Upwind (UP) stabilization function

$$(27d) \quad \Phi^{UP}(t) := t$$

- Scharfetter-Gummel (SG) stabilization function

$$(27e) \quad \Phi^{SG}(t) := t - 1 + \mathcal{B}(2t), \quad \mathcal{B}(t) := \frac{t}{e^t - 1}.$$

In the case where (27e) is adopted, the resulting stabilized DMH coincides with the classic SG exponentially fitted difference scheme (cf. [34]).

The accuracy of the two stabilized DMH methods, as $h \rightarrow 0$, is $\mathcal{O}(h)$ if $\Phi = \Phi^{UP}$ while is $\mathcal{O}(h^2)$ if $\Phi = \Phi^{SG}$. Thus, the SG formulation is far superior than the upwind method in the limit of a small grid size. However, for a large value of the Péclet number the two stabilized methods are practically equivalent in terms of the amount of added artificial diffusion (see also [33] and [24]).

8.1.3. *Matrix form of the stabilized DMH method.* Using superscripts $-$ and $+$ to refer to quantities on the interval $K_i^- = [x_{i-1}, x_i]$ and $K_i^+ = [x_i, x_{i+1}]$, respectively, let us enforce continuity of J_h at every interior node x_i ($i = 2, \dots, N-1$)

$$(28a) \quad J_2^- = J_1^+.$$

Then, combining equations (26c) and (26d) with condition (28a), we get

$$(28b) \quad -\lambda_i \frac{2D^-}{h} + \frac{(v^- + \frac{2D^-}{h})(g^- h^2 + 2\lambda_{i-1} D^- + 2\lambda_i D^-)}{4D^- + c^- h^2} \\ = \lambda_i \frac{2D^+}{h} + \frac{(v^+ - \frac{2D^+}{h})(g^+ h^2 + 2\lambda_i D^+ + 2\lambda_{i+1} D^+)}{4D^+ + c^+ h^2}.$$

By inspection on (28b) the entries of the stiffness matrix \mathcal{M} and of the load vector \mathbf{f} become:

$$(28ca) \quad \mathcal{M}_{i,i-1} = - \left(\frac{v}{2} + \frac{D(1+\Phi)}{h} \right) \frac{1}{1 + \frac{ch^2}{4D}}$$

$$(28cb) \quad \mathcal{M}_{i,i} = \frac{2D(1+\Phi)}{h} \left(\frac{1 + \frac{ch^2}{2D}}{1 + \frac{ch^2}{4D}} \right)$$

$$(28cc) \quad \mathcal{M}_{i,i+1} = \left(\frac{v}{2} - \frac{D(1+\Phi)}{h} \right) \frac{1}{1 + \frac{ch^2}{4D}}$$

$$(28cd) \quad f_i = \frac{gh}{1 + \frac{ch^2}{4D}}.$$

Proposition 3 (Discrete Maximum Principle in the non stabilized case). *Set $\Phi = 0$ and assume that*

$$(28d) \quad \mathcal{P}e_{loc} < 1.$$

Then, the stiffness matrix \mathcal{M} is an M-matrix.

Proof. Recalling that $v > 0$, it turns out that $\mathcal{M}_{i,i-1}$ is < 0 . Moreover, we have $\mathcal{M}_{i,i} > 0$ and $f_i > 0$. By inspection on $\mathcal{M}_{i,i+1}$ we see that if (28d) is satisfied then \mathcal{M} is an M-matrix and the DMP holds for the solution of (24c). \square

Condition (28d) may be too restrictive in the choice of the mesh size so that the following result may be a convenient remedy.

Proposition 4 (Discrete Maximum Principle in the stabilized case). *When $\Phi = \Phi^{UP}$ or $\Phi = \Phi^{SG}$, the stabilized DMH method satisfies the DMP irrespective of the value of $\mathcal{P}e_{loc}$.*

Proof. It is easy to verify that

$$\sum_{j=1,\dots,N} \mathcal{M}_{i,j} > 0$$

for every interior node ($i = 2, \dots, N-1$), and

$$\begin{aligned} \mathcal{M}_{1,1} + \mathcal{M}_{1,2} &> 0 \\ \mathcal{M}_{N-1,N-1} + \mathcal{M}_{N,N} &> 0 \end{aligned}$$

at boundary nodes. Then, the conclusion immediately follows by applying Theorem 4. \square

9. EXPERIMENTAL VALIDATION OF THE DMH METHOD

In this section we numerically verify the convergence and stability properties of the DMH method.

N_{el}	$\ u - u_h\ _{L^2}$	$\ \Pi_0 u - u_h\ _{L^2}$	$\ u - \lambda_h^*\ _{L^2}$	$\ u - \lambda_h^*\ _{\infty, h}$
10	4.77887e-01	2.21777e-01	1.30666e-01	8.64963e-02
20	1.91869e-01	6.25684e-02	3.38644e-02	2.22424e-02
40	8.63963e-02	1.61248e-02	8.54321e-03	5.60052e-03
80	4.18183e-02	4.06198e-03	2.14066e-03	1.40542e-03
160	2.07297e-02	1.01743e-03	5.35468e-04	3.51510e-04
320	1.03422e-02	2.54479e-04	1.33886e-04	8.78873e-05
640	5.16826e-03	6.36272e-05	3.34727e-05	2.19724e-05
1280	2.58377e-03	1.59073e-05	8.36820e-06	5.49311e-06
2560	1.29184e-03	3.97683e-06	2.09202e-06	1.37325e-06

TABLE 1. Various error norms for numerical solutions u_h and λ_h^* as a function of the number of intervals N_{el} . No stabilization is adopted.

N_{el}	$\ J - J_h\ _{L^2}$	$\ J - J_h\ _{H^1}$
10	3.28036e-01	2.60239e+00
20	8.75295e-02	1.30056e+00
40	2.16140e-02	6.47536e-01
80	5.29217e-03	3.23222e-01
160	1.30365e-03	1.61529e-01
320	3.23124e-04	8.07533e-02
640	8.04091e-05	4.03752e-02
1280	2.00543e-05	2.01874e-02
2560	5.00749e-06	1.00937e-02

TABLE 2. Error norms H^1 and L^2 for numerical solution J_h as a function of the number of intervals N_{el} . No stabilization is adopted.

9.1. Convergence Analysis. We consider the model BVP (18) with homogeneous BCs, $u(0) = u(L) = 0$, $d = 5$, coefficients $D = v = c = 1$, and $g(x) = e^{-x} [x^2 - (6 + L)x + 3L - 2]$ in such a way that the exact solution is the pair

$$u(x) = xe^{-x}(L - x), \quad J(x) = -e^{-x} [2x^2 + 2x(L - 1) + L].$$

In the numerical approximation of the problem, the mesh size is uniform and equal to $h = d/N_{el}$, with $N_{el} = [10, 20, 40, 80, 160, 320, 640, 1280, 2560]^T$. Table 1 illustrates the convergence history of the DMH method by reporting various error norms for $u - u_h$ and $u - \lambda_h^*$. The discrete maximum norm $\|\cdot\|_{\infty, h}$ associated with the triangulation \mathcal{T}_h is defined for each continuous function $\eta(x) : [0, L] \rightarrow \mathbb{R}$ as

$$\|\eta(x)\|_{\infty, h} := \max_{x_i \in \mathcal{N}_h} |\eta(x_i)|.$$

Table 2 reports the error $J - J_h$ in the L^2 -norm and in the $H_{\text{div}} \equiv H^1$ -norm.

The analysis of the asymptotic convergence orders that are predicted by Tables 1 and 2 show that the computed numerical solutions verify the following error estimates

- $\|u - u_h\|_{L^2} \leq Ch$
- $\|\Pi_0 u - u_h\|_{L^2} \leq Ch^2$
- $\|u - \lambda_h^*\|_{L^2} \leq Ch^2$
- $\|u - \lambda_h^*\|_{\infty, h} \leq Ch^2$

- $\|J - J_h\|_{H^1} \leq \mathcal{C}h$
- $\|J - J_h\|_{L^2} \leq \mathcal{C}h^2$

The above results are in excellent agreement with the theoretical convergence rates predicted in the elliptic case in [3] and [5, 29].

9.2. Reaction-Dominated and Advective-Dominated Regimes. In this section we demonstrate the efficacy of the stabilization techniques proposed in Sect. 8.1 in the study of two model problems, special instances of the BVP (18). For ease of presentation, we set $L = 1$ and we subdivide the computational domain into $N_{el} = 10$ uniform intervals of size $h = 1/N_{el} = 0.1$. We also assume that the coefficients D, v, c and g are constant, with $g = 1$ and we take homogeneous boundary conditions, $u(0) = u(1) = 0$ ($\bar{u} = 0$).

9.2.1. Diffusion-reaction BVP: mass-lumping. In this case we have $v = 0$. A barrier function for u is $\phi(x) = 1/c$. If the diffusion coefficient is small compared to the reaction term, e.g $D = 10^{-3}$, $c = 1$, spurious (unphysical) oscillations arise near the boundaries, see Figure 2(a). In order to eliminate such oscillations, we adopt the mass-lumping stabilization procedure. The numerical solution λ_h obtained with mass-lumping is illustrated in Figure 2(b).

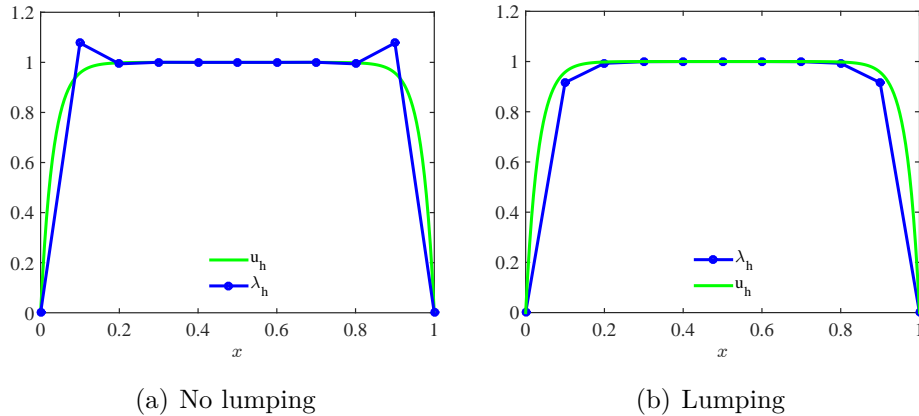


FIGURE 2. Exact and numerical solution of the diffusion-reaction BVP. Exact (green, solid line) and numerical solutions λ_h (blue line with bullets).

9.2.2. Diffusion-advection BVP: artificial diffusion. In this case we have $c = 0$. A barrier function for u is $\phi(x) = x/v$. If the diffusion coefficient is small compared to the advective term, e.g $D = 5 \cdot 10^{-3}$, $v = 1$, spurious (unphysical) oscillations arise in the neighborhood of $x = 1$ and propagate throughout the entire domain polluting the overall quality of the computed solution, see Figure 3(a). Numerical solutions λ_h obtained with UP and SG stabilization functions are illustrated in Figures 3(b) and 3(c), respectively. In the case of the SG stabilization function, the computed λ_h is *nodally exact*.

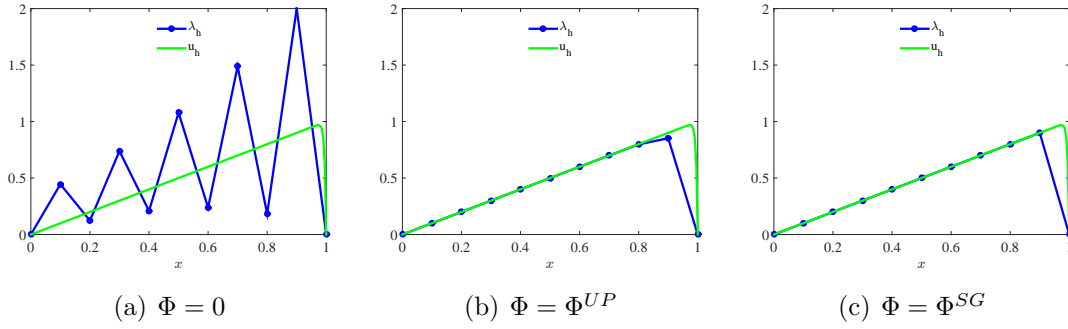


FIGURE 3. Exact and numerical solution of the diffusion-advection BVP. Exact (green, solid line) and numerical solutions λ_h (blue line with bullets).

10. SIMULATION OF BIOLOGICAL CHANNELS

In this concluding section we carry out a thorough validation of the vET and vTHD models in the study of two different biological channels: 1) the Gramicidin-A channel considered in [10]; and 2) the bipolar nanofluidic diode considered in [40]. The main focus of the simulations is on the current-voltage (IV) characteristics of the channel and on how the IV curves are affected by the boundary conditions, especially the temperature of the two bulk regions, $T(0) = T_L$ and $T(d) = T_R$. Also, we aim to investigate the electroosmosis effect, which is accounted for by the electrolyte fluid velocity v_e . In all the reported computations we set $N_{el} = 200$ and use the SG stabilization function (27e), with the exception of a specific case discussed in Section 10.1. Moreover, in the case of the vTHD model we set the saturation velocity v_{sat} equal to 10 ms^{-1} . We also assume that the channel has a constant cross-sectional area equal to \mathcal{A} , whose value may vary from channel to channel. For further information on the simulated channels, we suggest to consult [24] and the references cited therein.

10.1. Gramicidin-A channel (ballistic diode). This channel is thoroughly analyzed in the work [10] that is here used as a benchmark for the biophysical and numerical assessment of models and methods proposed in the present article. To allow comparison between the results of our models and those of [10] we set $v_e = 0$. Unless otherwise specified, the subsequent figures refer to computations with the THD model, meaning that the outcome of the ET model would appear indistinguishable. The channel length d is equal to 2.5 nm , φ_R is always set equal to 0 V and $\varphi_L = V_{app}$, V_{app} being the externally applied voltage.

10.1.1. Electrochemical variables. The permanent charge profile of the channel is illustrated in Fig. 4 (left). Because of the negative fixed charge the channel is highly selective to ion flow and attracts positive Na^+ ions while Cl^- ions are mainly repelled. This behavior is confirmed by the computed ion concentration profiles shown in Fig. 4 (right) in the case where a voltage drop $\varphi_L - \varphi_R = V_{app} = 0.1 \text{ V}$ is applied across the channel. We first observe that the cation concentration computed by our algorithm is in excellent agreement with that of [10]. We also notice the presence of strong internal layers in the Na^+ distribution which are effectively captured by the stabilized DMH discretization without introducing spurious oscillations. In

the mentioned reference [10] the hydrodynamic equations are solved using a rather different numerical strategy based on the essentially non oscillatory finite differences with shock capturing introduced in [37, 38]. The role of the SG stabilization in the quality of the computed ion concentrations is well documented by the results shown in Fig. 5. In this graph, we see on the left side the cation and anion densities obtained by running the DMH discretization scheme without stabilization ($\Phi = 0$) on an uniform grid of $N_{el} = 19$ elements. The maximum local Péclet number is in this case equal to 68.6288 so that the solution exhibits a markedly oscillatory behavior and fails to satisfy the DMP. Conversely, the adoption of the SG stabilization with the same number of elements produces the ion concentrations plotted on the right side of Fig. 5. The computed solution is strictly positive and the internal layers at the interfaces between the channel and highly doped regions are captured with the resolution allowed by the roughness of the grid size.

Permanent charge and concentrations

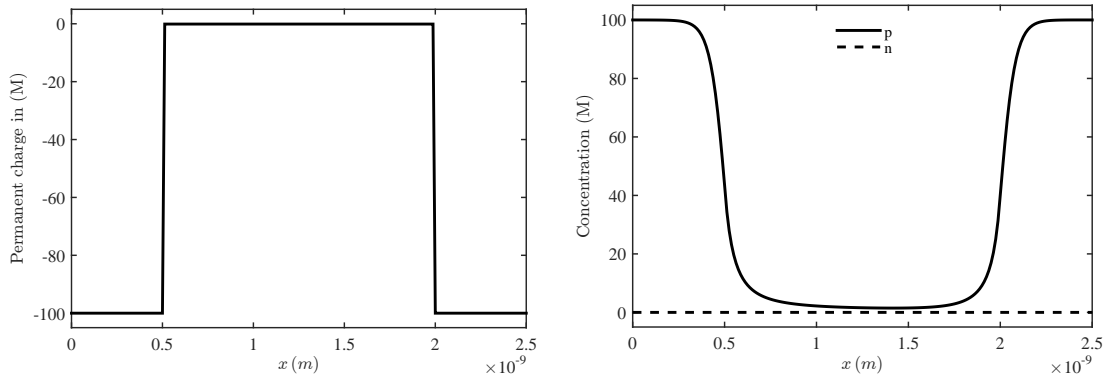


FIGURE 4. Gramicidin-A channel. Left: permanent charge profile. Right: ion concentrations.

The permanent charge profile and the consequent distribution of ions allows us to regard the Gramicidin-A channel as the biophysical analogue of an electronic "ballistic" diode of type p^+-p-p^+ . This analogy is useful in the interpretation of simulation results and supports the idea that "channels are transistors alive" (cf. [12]). In this respect, the region of the channel $x \in [0, 0.5]$ nm corresponds to the Source terminal which has the role of emitting cations into the channel, while the region of the channel $x \in [2, 2.5]$ nm corresponds to the Drain terminal which has the role of collecting the cations that have travelled throughout the channel under the action of the thermo-electro-chemical forces. Electric potential and electric field profiles are shown in Fig. 6 (left) and Fig. 6 (right), respectively. Again, we observe that the electric potential and field computed by our algorithm are in excellent agreement with those of [10]. By inspection of the electric potential distribution, we see that the positive pole of the bio-electrical system is located at $x = 0$, nm while the negative pole is at $x = 2.5$ nm. Thus, the cations move from left to right, giving rise to accumulation of (fixed) negative charge at the entrance of the channel and positive (mobile) charge at the outlet of the channel. These accumulations correspond to the two strong peaks visible in the electric field distribution.

To investigate the effect of different boundary values for the temperature at both entrance and outlet of the channel we let $T(0) = T(d)$ range between 270 K and

Concentration profile without and with numerical stabilization

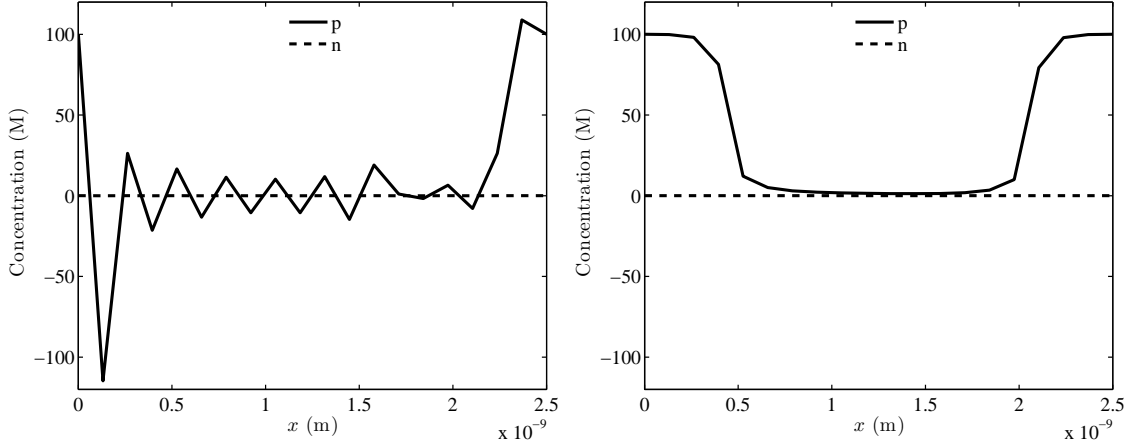


FIGURE 5. Gramicidin-A channel. Concentration profile with a grid of 19 elements. When no numerical stabilization is adopted, spurious oscillations arise (left). The SG stabilization (right) leads to a stable solution.

Potential and electric field

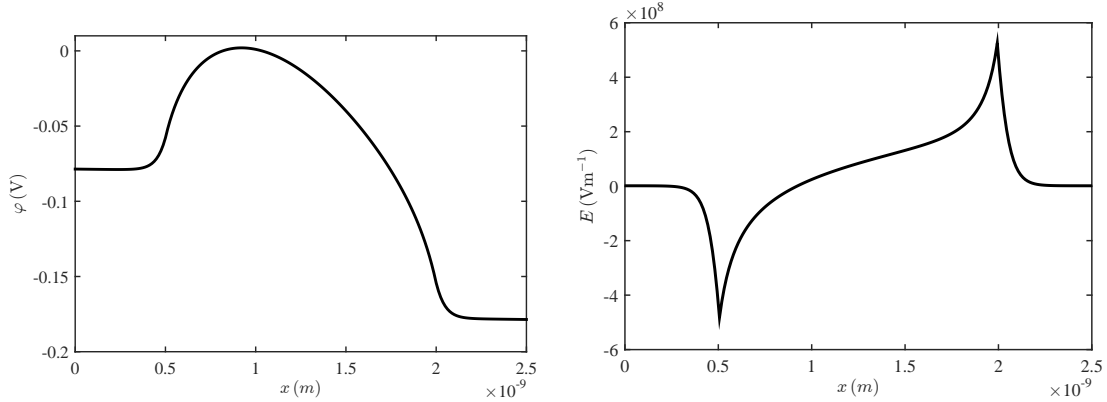


FIGURE 6. Gramicidin-A channel. Left: electric potential. Right: electric field.

330 K. Fig. 7 shows the IV curves for the THD model (left) and the ET model (right), respectively. The externally applied voltage V_{app} ranges from 0 to 0.1 V. Temperature influence is visible in both models: the higher the bath temperature the lower the current. This agrees with the biophysical insight that an increase of bath temperature corresponds to a higher thermal energy for the ions and, consequently, to a higher energy dissipation because of frictional effects between particles and fluid. We notice also that the ET model predicts a slightly higher current than the THD model because this latter model accounts for convective energy dissipation within the fluid.

10.1.2. *Thermal variables.* Cation temperature profiles when $T(0)$ and $T(d)$ are increased separately, are shown in Fig. 8.

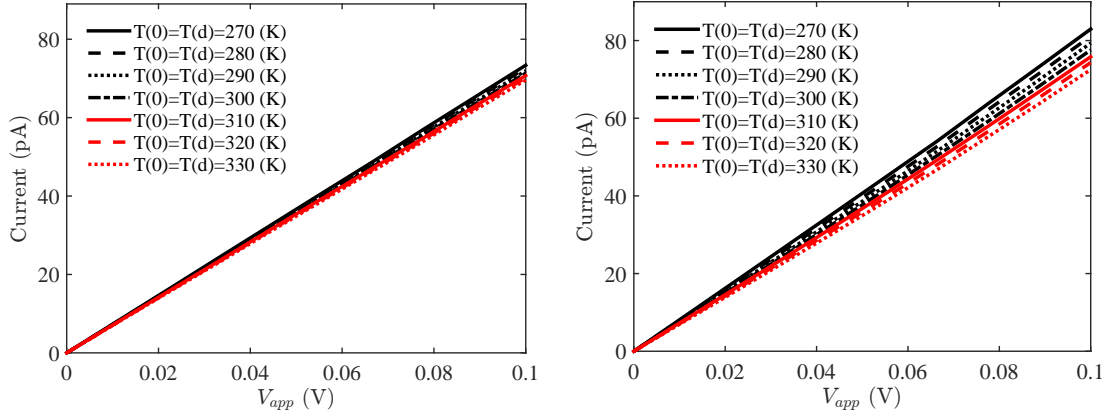
IV curves when $T(0) = T(d) \neq 300$ K

FIGURE 7. Gramicidin-A channel. IV curves when $T(0) = T(d) \neq 300$ K (left). THD model (left). ET model (right).

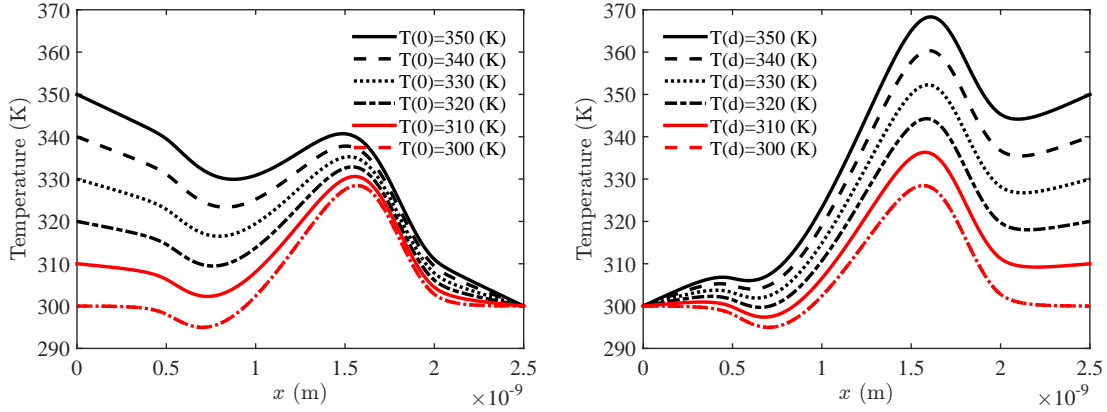
Ion temperature when $T(0)$ or $T(d) > 300$ K

FIGURE 8. Gramicidin-A channel. Cation temperature profiles. $T(0) > 300$ K (left). $T(d) > 300$ K (right).

Looking at the two families of distributions, we can distinguish five distinct subregions in each curve: the Source and Drain regions (reservoirs), the channel region and the two junctions separating Source and Drain from the ion channel. In the two reservoirs, the temperature profile is linear, because the cation concentration is almost constant and the electric field is very small. Then, ion temperature increases in the channel region according with the fact that particles are accelerated by the electric field from left to right, approximately for $x \geq 0.8$ nm (cf. Fig. 6, right). However, the effect of the electric field at the two junctions is quite different in the two sets of thermal boundary conditions. If $T(0) > T(d)$, electric and thermal fields act in the same direction (from left to right) so that as $T(0)$ increases, the thermal flow at the two channel boundaries correspondingly increases. If $T(d) > T(0)$ electric and thermal forces act in opposite directions and this contributes to diminishing the thermal flow at the two channel boundaries. It is interesting to notice that ion heating (i.e., the maximum value of ion temperature inside the channel) is considerably larger

in the case where $T(d) > T(0)$, because in this condition ion acceleration due to the electric field greatly dominates over the thermal field along the channel (moving from left to right) so that the ion total energy increases and temperature gets larger. Then, once the ions are injected across the junction between channel and Drain they immediately thermalize to the local energy of the reservoir distribution and approximately cool down to the temperature enforced at $x = d$.

Electrolyte fluid temperature when $T(0)$ or $T(d) > 300$ K

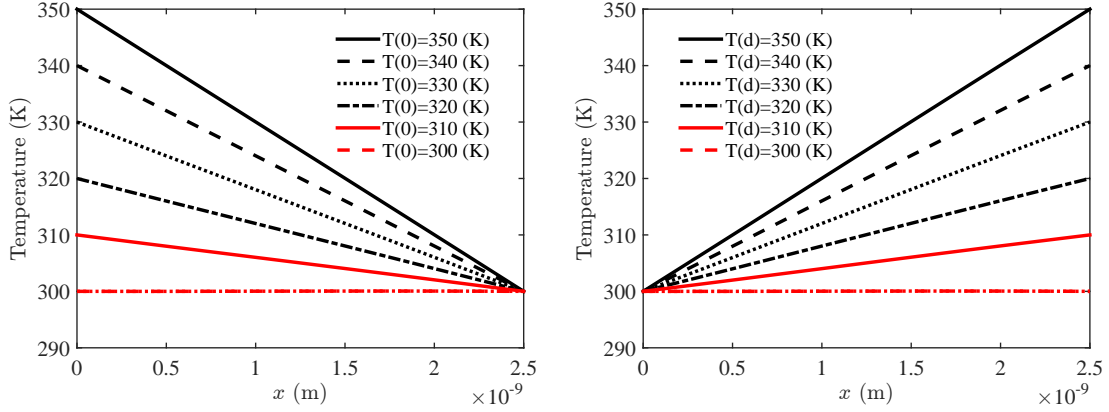


FIGURE 9. Gramicidin-A channel. Electrolyte fluid temperature profiles. $T(0) > 300$ K (left). $T(d) > 300$ K (right).

Temperature profiles of the electrolytic fluid are almost linear for both choices of the applied thermal drop, see Fig. 9. This behaviour is to be ascribed to the high value of thermal conductivity of the electrolyte fluid compared to that of the ion fluid. This makes the fluid behave as a perfect sink so that its heating is only passively driven by an external temperature gradient according to Fourier's law (9f) ($v_e = 0$ in this case).

10.1.3. *Ion velocity.* From ion velocity profiles we can inspect how an externally applied temperature gradient may affect ion motion in the channel.

Ion velocity when $T(0)$ or $T(d) > 300$ K. THD model

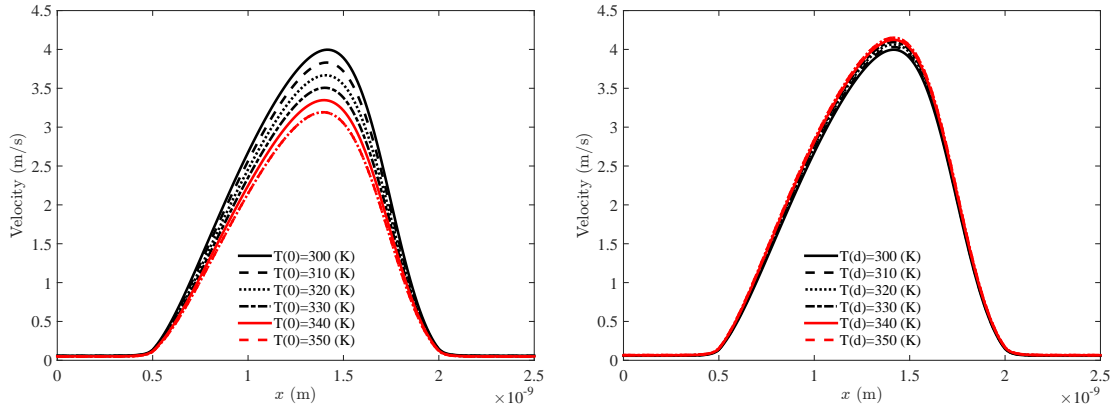


FIGURE 10. Gramicidin-A channel. Cation velocity computed by the THD model. $T(0) > 300$ K (left), $T(d) > 300$ K (right).

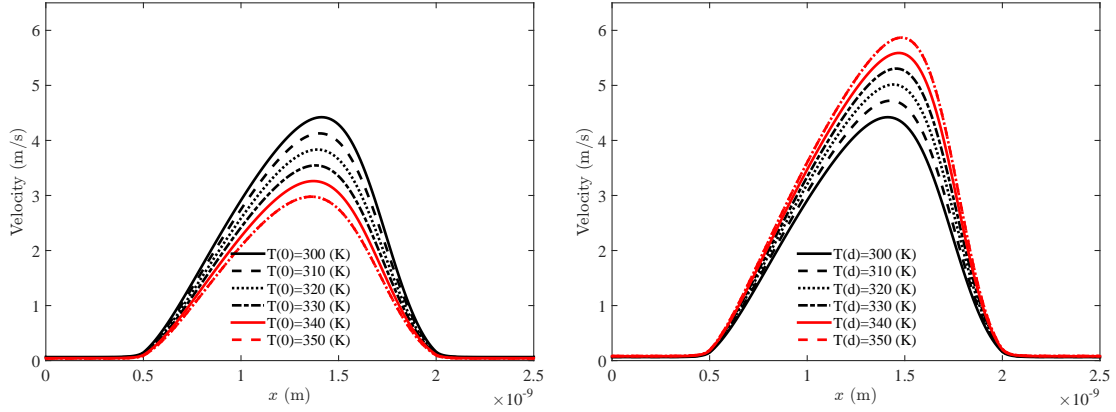
Ion velocity when $T(0)$ or $T(d) > 300$ K. ET model

FIGURE 11. Gramicidin-A channel. Cation velocity computed by the ET model. $T(0) > 300$ K (left), $T(d) > 300$ K (right).

In Fig. 10 (left) we see ions moving slower when $T(0) > T(d) = 300$ K. The opposite happens in Fig. 10 (right) where $T(d) > T(0) = 300$ K. However, in this latter case, velocity variations are much smaller. Again, the different behavior of the ion velocity in the two sets of thermal conditions is related to the interplay between electric and thermal forces already discussed in Sect. 10.1.2. If $T(0) > T(d)$ thermal diffusion is larger than in the case where $T(d) > T(0)$, and increases as $T(0)$ increases. This explains the maximum value of v_n at $T(0) = 300$ K. If $T(d) > T(0)$ ion motion is mainly driven by the electric field, which explains why the various curves are substantially insensitive to the increase of $T(d)$. The ion velocity in the ET model exhibits a trend similar to that of the THD model, see Fig. 11, even if the distribution of the peak value shows a much larger spread than in the case of the velocity computed by the THD model. This is to be ascribed to the larger thermal conductivity of the (thermally) unified system composed by anions, cations and fluid.

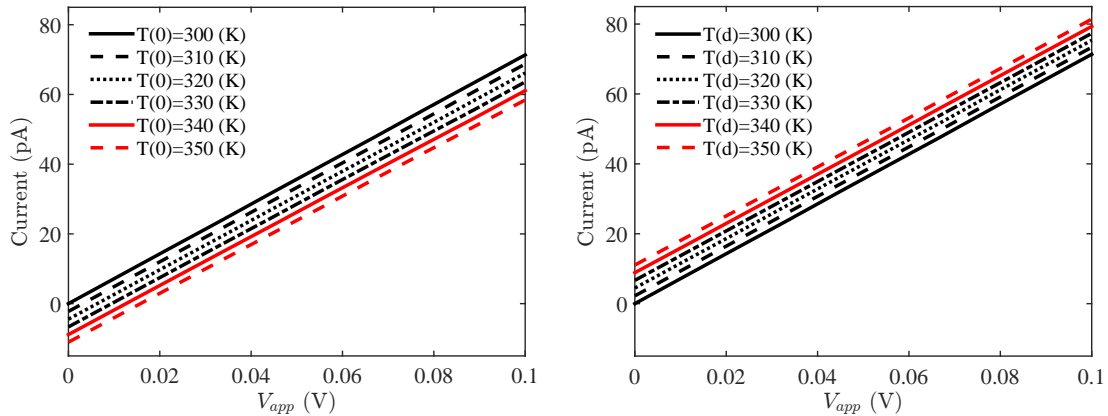
IV curve when $T(0)$ or $T(d) > 300$ K. THD model

FIGURE 12. Gramicidin-A channel. I-V curves computed by the THD model. $T(0) > 300$ K (left), $T(d) > 300$ K (right).

IV curve when $T(0)$ or $T(d) > 300$ K. ET model

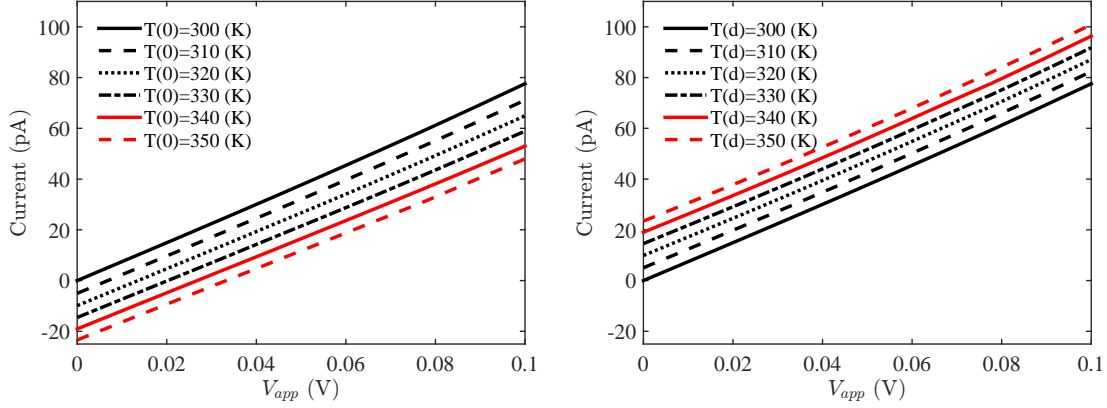


FIGURE 13. Gramicidin-A channel. I-V curves computed by the ET model. $T(0) > 300$ K (left), $T(d) > 300$ K (right).

The IV curves computed by the two models in the two distinct thermal sets of boundary conditions reflect what reported about ion velocities: a smaller ion velocity means a smaller current flowing in the channel. The externally applied voltage V_{app} ranges from 0 to 0.1 V. Fig. 12 (left) shows the IV curves for the THD model when $T(0) > T(d) = 300$ K. Notice that the current assumes negative values when V_{app} is close to zero and the temperature gradient due to thermal BCs is strong enough to counterbalance the affect of the applied voltage. Consistently with the ion velocity profiles of Fig. 10 (left), the current flowing in the channel is lower than in the case of homogeneous thermal BCs. As $T(0)$ increases, the I-V profile is shifted down with respect to the case of homogeneous BCs ($T(0) = 300$ K solid black line). The case when $T(d) > T(0) = 300$ K is shown in Fig. 12 (right). In this situation the IV relationships are shifted up, meaning that as $T(d)$ increases, a higher current flows in the channel, just as predicted from the ion velocity profiles of Fig. 10 (right). Similar results and observations hold for the IV curves predicted by the ET model, see Figs. 13.

10.2. IV curves with velocity extended THD and ET models. In the simulations conducted so far, we set $v_e = 0$, which corresponds to neglecting the electroosmosis effect. We have also conducted simulations with v_e varying in the range $0 \div 0.01 \text{ m s}^{-1}$, and we found that it has no appreciable influence on the current flowing in the channel, so that no results are shown in this case. However, different conclusions are drawn in the channel presented in the following section.

10.3. Bipolar nanofluidic diode. The nanofluidic channel investigated in the present section (whose detailed representation can be found in [40, 24]) is called Bipolar (BP) nanofluidic diode because of its similarity with a p - n electronic diode: as a matter of fact, the BP channel can operate into two different states, depending on the sign of the applied voltage: (1) an 'open' state (also called 'forward' bias), characterized by high current flowing through the device, and (2) a 'closed' state (also called 'reverse' bias), with very little current flowing in the channel.

10.3.1. Electrochemical variables. The input-output behavior of the BP channel is related to the surface permanent charge profile (cf. Fig. 1). The channel has a

negative surface charge along half of its length, while the remaining part has positive surface charge (of the same magnitude), see Fig. 14 (left). Thus, anions and cations carry equal weight to channel behavior. This is confirmed by the symmetric spatial distribution of ion concentrations, both in the case of forward and reverse bias, see Fig. 14 (middle) and Fig. 14 (right), respectively. Notice that ion concentration is much higher in forward bias than reverse bias. Electric potential and electric field profile are shown in Fig. 15. One can see that, in the closed-state, carrier flow is inhibited by the potential barrier at the middle of the channel. Conversely, in the open-state, the potential drop enhances ion flow. The computed IV curves show the on-off trend just described. In particular, we see that if V_{app} is negative the current is almost equal to zero, while it increases in a nonlinear manner if V_{app} is positive (cf. Fig. 16). The predicted marked on-off function mode of the BP channel and the shape of the I-V curves are also in very good qualitative agreement with data reported in the study of heat biosensors in [7, 41, 39]. This fact is an encouraging motivation to a further use and calibration of the computational models and methodologies proposed in the present article on biophysical novel applications.

Permanent charge and concentrations

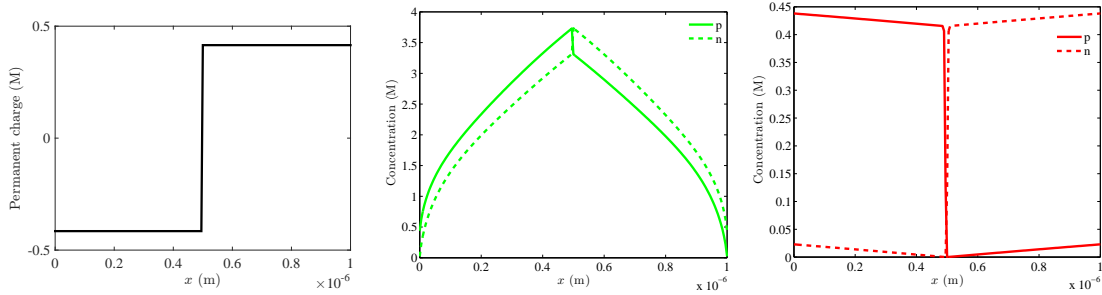


FIGURE 14. BP channel. Permanent charge profile (left). Ion concentrations: forward bias $V_{app} = +1$ V (middle), reverse bias $V_{app} = -1$ V (right).

10.3.2. *Temperature.* The IV curves, when $T(0) = T(d)$ assumes lower or higher values than the reference value of 300 K, are shown in Fig. 16 for the THD model (left) and ET model (right), respectively. The externally applied voltage V_{app} ranges from -1 to 1 V. The IV curves computed by the THD model follow the same trend, as a function of the bath temperature, as in Sect. 10.1 (cf. Fig. 7): the higher the bath temperature the lower the current flowing in the channel because of increased frictional effects, see Fig 16 (left). The IV curves computed by the ET model in this type of channel differ remarkably from those computed by the THD model with respect to boundary temperature: the higher the bath temperature, the higher the current, see Fig 16 (right). We also observe that the spread in the value of the maximum channel current as a function of bath temperature is much wider for the THD model than for the ET model. This trend was exactly the opposite in the simulation of the Gramicidin-A channel of Sect. 10.1, as demonstrated by Fig. 7. We point out that the application to the BP channel of the theoretical prediction for channel current given by the ideal diode model (see, e.g., [27]) would yield

$$(4) \quad I = I_0 \left[\exp \left(\frac{qV_{app}}{K_B T_{sys}} \right) - 1 \right]$$

Potential and electric field

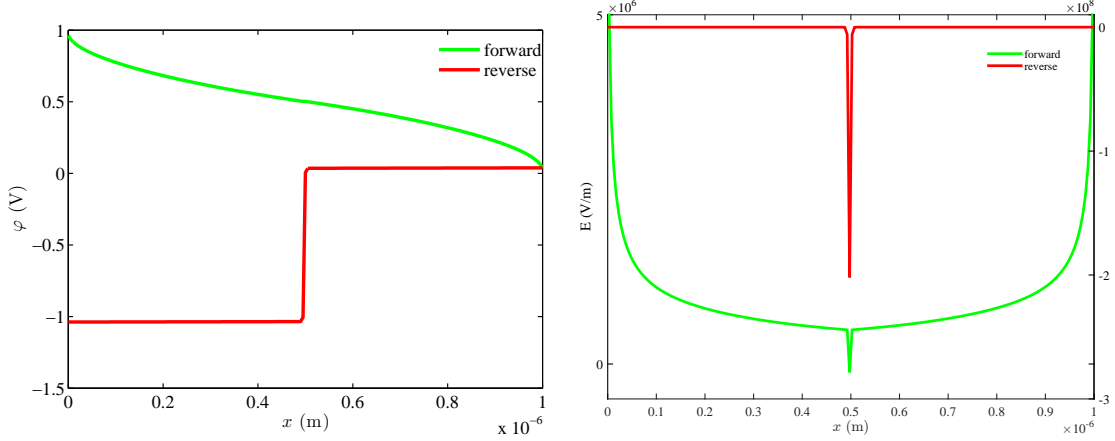


FIGURE 15. BP channel. Electric potential profile: forward (green) and reverse (red) bias. Electric field profiles: forward bias (green, left axis scale) and reverse (red, right axis scale).

IV curves when $T(0) = T(d) \neq 300$ K

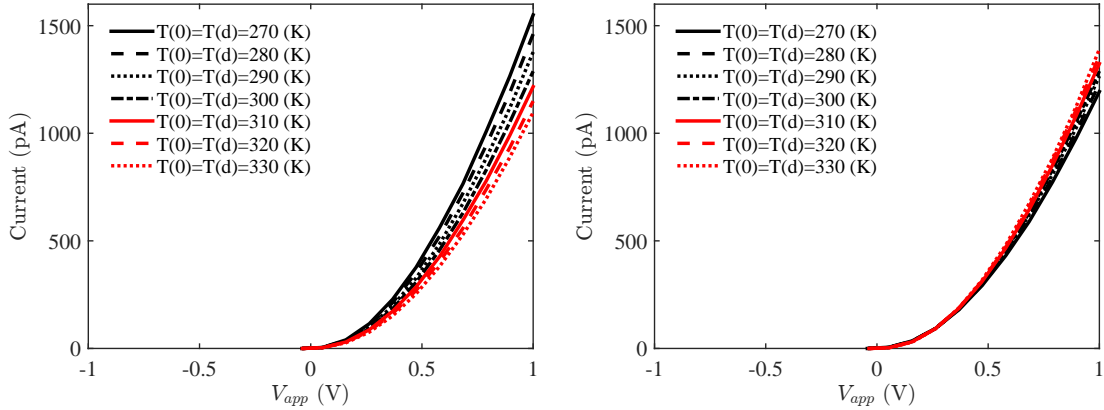


FIGURE 16. BP diode. IV curves when $T(0) = T(d) \neq 300$ K: THD model (left), ET model (right).

where I is the total current flowing in the diode and I_0 is the saturation current. Thus, according to (4), an increase of channel system temperature turns out into a decrease in channel current, in accordance with the results computed by the THD model. Despite this preliminary indication in favor of the predictions of the THD model, we feel that the strongly different response of the two models when applied to different channel configurations certainly warrants further investigation and will be the object of a further step of our research activity.

Also the temperature profiles of electrolytic fluid differ between the ET model and the THD model. The profiles from ET model have a non linear profile, while those from THD model are linear, see Fig. 17 (left) and Fig. 17 (right), respectively, when $T(0)$ ranges from 270 to 330 K.

10.3.3. Electroosmosis. In this type of channel the influence of the electrolytic fluid velocity is shown in Fig 18 (left) for the vTHD model and in Fig. 18 (right) for

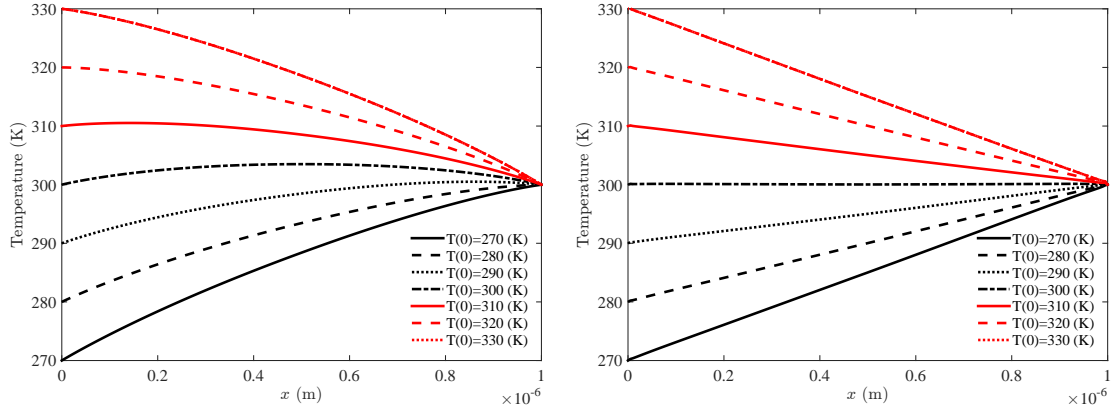
$T_e(x)$ profile when $T(0) \neq 300$ K

FIGURE 17. BP diode. Water temperature in the ET model (left) and THD model (right).

the vET model. The selected range for the electrolyte fluid velocity (v_e from 0 to 0.01 m/s) is rather arbitrary since our model does not account, at the moment, for a self-consistent coupling between the vTHD system and the NS equations for the fluid. As the fluid velocity has positive sign, electrolytic particles flow from left to right. Accordingly, this additional translational force should enhance the movement of positive ions, while it should reduce that of negative ions, since the two ions move in opposite directions. From the IV curves shown, one can see that the additional driving force due to v_e lowers the total current flowing in the channel in both models. Analogous results hold for negative values of v_e (not shown).

The temperature of the electrolytic fluid velocity for different values of v_e is shown in Fig. 19. Temperature is only partially affected by v_e . The increase in temperature predicted by the vET model (left) is about 3 K, which is quite remarkable, especially if compared to the results obtained with the vTHD model (middle), where temperature changes are much less significant, instead. The very different prediction of the vTHD formulation is related to the parameter v_{sat} that strongly affects the value of the relaxation time parameter τ_{w_ν} (cf. (11b)) in the energy balance equation (9c): the larger v_{sat} , the smaller τ_{w_ν} , which corresponds to almost instantaneous restoration of equilibrium conditions in the electrolyte. Indeed, taking a smaller value of the saturation velocity, for example $v_{sat} = 1$ m/s, leads to a result that is much closer to the thermal profile predicted by the vET model, see Fig. 19 (right).

11. CONCLUSIONS AND RESEARCH PERSPECTIVES

In the present article we have proposed and numerically investigated a hierarchy of mathematical models for the simulation of thermal, fluid and electrochemical phenomena in biological transmembrane channels. The hierarchy is an extension of the classic Poisson-Nernst-Planck model for ion electrodiffusion and is conducted along the same lines of thought that have guided the development of the so-called hydrodynamic transport model in the analysis of semiconductor devices. To discretize the proposed models we have devised in the 1D case a robust finite element dual-mixed hybridized method that ensures flux conservation, self-equilibrium and satisfaction of a positivity principle for ion concentrations and temperatures. The numerical scheme

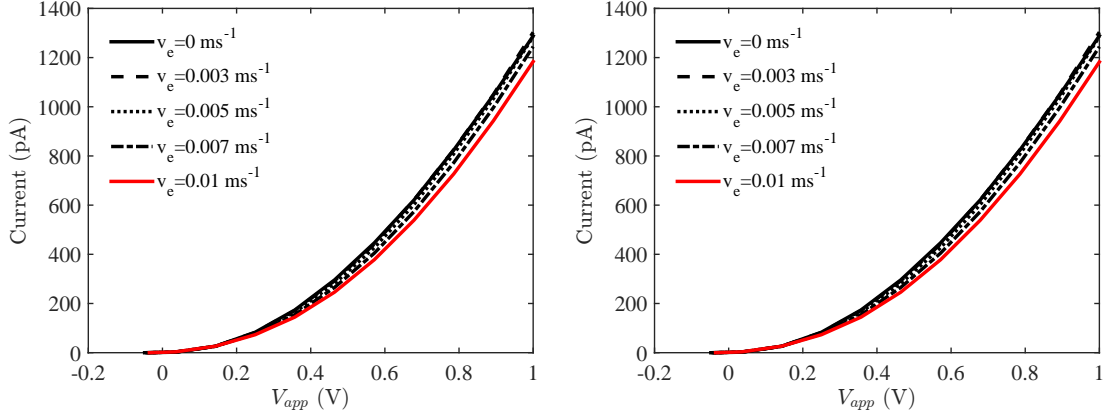
IV curves when $v_e > 0$ m/s

FIGURE 18. BP diode. IV curve when v_e ranges in $0 \div 0.01$ m/s. vTHD model (left). vET model (right).

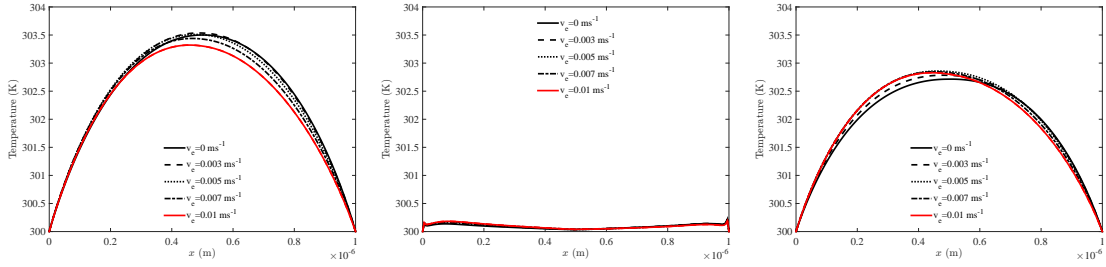
 $T_e(x)$ profile for different v_e (vET vs. vTHD)

FIGURE 19. BP diode. v_e ranges in $0 \div 0.01$ ms^{-1} . vET model (left) differs greatly from vTHD at $v_{sat} = 10$ m/s (middle), while is quite close to vTHD at $v_{sat} = 1$ m/s.

has been thoroughly studied in several benchmark problems that demonstrate its accuracy and stability. An appropriate solution map is used to successively solve the nonlinear system of equations arising from model hierarchy and the resulting computational tool has been successfully calibrated and validated in the simulation of two realistic biological channels. Future developments of this study include:

- time dependent simulations to describe the response of the channel to externally applied stimuli;
- self-consistent coupling of the hierarchy with the solution of the Navier-Stokes equations for the electrolyte fluid;
- deeper investigation of the dependence of model predictions on biophysical parameters, for instance, saturation velocity that seems to play a critical role in determining the self-heating effect in the electrolyte fluid;
- extension of the numerical scheme to 2D and 3D channel simulation.

REFERENCES

- [1] A. Abramo, R. Brunetti, C. Fiegna, C. Jacoboni, B. Riccò, E. Sangiorgi, and F. Venturi. Monte Carlo simulation of silicon devices. In G. Baccarani, editor, *Process and Device Modeling for Microelectronics*, chapter 2, pages 155–216. Elsevier, 1993.

- [2] T. Arbogast and Z. Chen. On the implementation of mixed methods as nonconforming methods for second-order elliptic problems. *Math. Comput.*, 64(211):943–972, July 1995.
- [3] D.N Arnold and F. Brezzi. Mixed and nonconforming finite element methods: implementation, postprocessing and error estimates. *Math. Modeling and Numer. Anal.*, 19(1):7–32, 1985.
- [4] G. Baccarani, M. Rudan, R. Guerrieri, and P. Ciampolini. Process and device modeling. chapter Physical models for numerical device simulation, pages 107–158. North-Holland Publishing Co., Amsterdam, The Netherlands, The Netherlands, 1986.
- [5] F. Brezzi and M. Fortin. *Mixed and Hybrid Finite Element Methods*. Springer Verlag, New York, 1991.
- [6] A. N. Brooks and T. J.R. Hughes. Streamline Upwind/Petrov-Galerkin formulations for convection dominated flows with particular emphasis on the incompressible Navier-Stokes equations. *Computer Methods in Applied Mechanics and Engineering*, 32(120133):199 – 259, 1982.
- [7] M. J. Caterina, M. A. Schumacher, M. Tominaga, T. A. Rosen, J. D. Levine, and D. Julius. The capsaicin receptor: a heat-activated ion channel in the pain pathway. *Nature*, 389(6653):816–824, October 1997.
- [8] D. P. Chen and R. S. Eisenberg. Charges, currents, and potentials in ionic channels of one conformation. *Biophysical journal*, 64(5):1405–1421, 1993.
- [9] D. P. Chen and R. S. Eisenberg. Flux, coupling, and selectivity in ionic channels of one conformation. *Biophysical journal*, 65:727–746, 1993.
- [10] D.P. Chen, R.S. Eisenberg, J.W. Jerome, and C.W. Shu. Hydrodynamic model of temperature change in open ionic channels. *Biophysical Journal*, 69(6):2304 – 2322, 1995.
- [11] J Douglas and J. E. Roberts. Global estimates for mixed methods for second order elliptic equations. *Math. Comp.*, 44:39–52, 1985.
- [12] R. S. Eisenberg. Ions in fluctuating channels: transistors alive. *Fluctuations and Noise Letters*, 11:76–96, 2005.
- [13] G. B. Ermentrout and D. H. Terman. *Mathematical Foundations of Neuroscience*. Springer, 2010.
- [14] H. L. Fields. *Pain*. McGraw-Hill, New York, 1987.
- [15] K. Hess, U. Ravaioli, N.R. Aluru, M. Gupta, and R.S. Eisenberg. Simulation of biological ionic channels by technology computer-aided design. In *Computational Electronics, 2000. Book of Abstracts. IWCE Glasgow 2000. 7th International Workshop on*, pages 70–, May 2000.
- [16] B. Hille. *Ionic Channels of Excitable Membranes*. Sinauer Associates, Inc., Sunderland, MA, 2001.
- [17] S. Hu and K. Hess. An application of the recombination and generation theory by Shockley, Read and Hall to biological ion channels. *Journal of Computational Electronics*, 4(1-2):153–156, 2005.
- [18] J.W. Jerome. *Analysis of charge transport*. Springer-Verlag, 1996.
- [19] J.W. Jerome. Analytical approaches to charge transport in a moving medium. *Transport Theory and Statistical Physics*, 31:333–366, 2002.
- [20] J.W. Jerome and R. Sacco. Global weak solutions for an incompressible charged fluid with multi-scale couplings: Initial-boundary value problem. *Nonlinear Analysis*, 71:e2487–e2497, 2009.
- [21] A. Juengel. *Transport Equations for Semiconductors*. Number 773 in Lecture Notes in Physics. Springer, Berlin, 2009.
- [22] J. P. Keener and J. Sneyd. *Mathematical Physiology*. Springer, New York, 1998.
- [23] T. Kerkhoven and Y. Saad. On acceleration methods for coupled nonlinear elliptic systems. *Numerische Mathematik*, 60:525–548, 1992.
- [24] F. Manganini. Thermo-electro-chemical modeling and simulation of ion transport in nanochannels. Master’s thesis, Politecnico di Milano, 2013. https://www.politesi.polimi.it/bitstream/10589/88365/1/Tesi_LM_770306_Fabio_Manganini.pdf.
- [25] P.A. Markowich. *The Stationary Semiconductor Device Equations*. Computational Microelectronics. Springer-Verlag, 1986.
- [26] P.A. Markowich, C.A. Ringhofer, and C. Schmeiser. *Semiconductor Equations*. Springer-Verlag, 1990.
- [27] R.S. Muller and T.I. Kamins. *Device Electronics for Integrated Circuits*. Wiley, 2002.

- [28] S. Pandey, A. Bortei-Doku, and M. H. White. Simulation of biological ion channels with technology computer-aided design. *Computer Methods and Programs in Biomedicine*, 85(1):1 – 7, 2007.
- [29] J.E. Roberts and J.M. Thomas. Mixed and hybrid methods. In P.G. Ciarlet and J.L. Lions, editors, *Finite Element Methods, Part I*. North-Holland, Amsterdam, 1991. Vol.2.
- [30] H. G. Roos, M. Stynes, and L. Tobiska. *Robust Numerical Methods for Singularly Perturbed Differential Equations*. Springer-Verlag Berlin Heidelberg, 2008.
- [31] I. Rubinstein. *Electrodiffusion of Ions*. SIAM, Philadelphia, PA, 1990.
- [32] M. Rudan, A. Gnudi, and W. Quade. A generalized approach to the hydrodynamic model of semiconductor equations. In G. Baccarani, editor, *Process and Device Modeling for Microelectronics*, chapter 2, pages 109–154. Elsevier, 1993.
- [33] R. Sacco and F. Saleri. Stabilized mixed finite volume methods for convection-diffusion problems. *East West J. Numer. Math.*, 5(4):291–311, 1997.
- [34] D.L. Scharfetter and H.K. Gummel. Large signal analysis of a silicon Read diode oscillator. *IEEE Trans. Electron Devices*, ED-16(1):64–77, 1969.
- [35] M. Schmuck. Analysis of the Navier-Stokes-Nernst-Planck-Poisson system. *Mathematical Models and Methods in Applied Sciences*, 19(6):993–1015, 2009.
- [36] S. Selberherr. *Analysis and Simulation of Semiconductor Devices*. Springer-Verlag, 1984.
- [37] C.W. Shu and S. Osher. Efficient implementation of essentially non-oscillatory shock-capturing schemes. *Journal of Computational Physics*, 77(2):439 – 471, 1988.
- [38] C.W. Shu and S. Osher. Efficient implementation of essentially non-oscillatory shock-capturing schemes, {II}. *Journal of Computational Physics*, 83(1):32 – 78, 1989.
- [39] L. Vay, C. Gu, and P.A. McNaughton. The thermo-trp ion channel family: properties and therapeutic implications. *British Journal of Pharmacology*, 165(4):787–801, 2012.
- [40] I. Vlassiuk, S. Smirnov, and Z.S. Siwy. Nanofluidic ionic diodes. comparison of analytical and numerical solutions. *ACS Nano*, 2(8):1589–1602, 2008.
- [41] T. Voets, G. Droogmans, U. Wissenbach, A. Janssens, V. Flockerzi, and B. Nilius. The principle of temperature-dependent gating in cold- and heat-sensitive TRP channels. *Nature*, 430(7001):748–754, 2004.

¹ DIPARTIMENTO DI MATEMATICA, POLITECNICO DI MILANO, PIAZZA L. DA VINCI 32, 20133 MILANO, ITALY, ² ISTITUTO DI MATEMATICA APPLICATA E TECNOLOGIE INFORMATICHE,, CNR, VIA E. BASSINI, 15, 20133 MILANO, ITALY, ³ NORTHWESTERN UNIVERSITY, MATHEMATICS DEPARTMENT, 2033 SHERIDAN ROAD EVANSTON, IL 60208-2730, USA